BEILSTEIN JOURNAL OF NANOTECHNOLOGY

Sustainable nanomaterials for energy conversion and environmental remediation

Edited by Pablo Jiménez Calvo, Ujjal K. Gautam and Lucia Helena Mascaro

Generated on 10 November 2026, 20:25

Imprint

Beilstein Journal of Nanotechnology
www.bjnano.org
ISSN 2190-4286
Email: journals-support@beilstein-institut.de

The *Beilstein Journal of Nanotechnology* is published by the Beilstein-Institut zur Förderung der Chemischen Wissenschaften.

Beilstein-Institut zur Förderung der Chemischen Wissenschaften
Trakehner Straße 7–9
60487 Frankfurt am Main
Germany
www.beilstein-institut.de

The copyright to this document as a whole, which is published in the *Beilstein Journal of Nanotechnology*, is held by the Beilstein-Institut zur Förderung der Chemischen Wissenschaften. The copyright to the individual articles in this document is held by the respective authors, subject to a Creative Commons Attribution license.

BEILSTEIN JOURNAL OF NANOTECHNOLOGY

Glycerol photoelectrochemical oxidation reaction at carbon nitrides/$BiVO_4$ materials

Charles Garcia da Cunha, Isabelle M. D. Gonzaga, Cristian Hessel, Izadora F. Reis, Ivo F. Teixeira, Lucia H. Mascaro and Elton Sitta*

Full Research Paper

Open Access

Address:
Federal University of São Carlos, São Carlos, SP, Brazil

Email:
Elton Sitta* - esitta@ufscar.br

* Corresponding author

Keywords:
biomass valorization; bismuth vanadate; glycerol valorization; heterojunctions; photoelectrochemistry

Beilstein J. Nanotechnol. **2026,** *17,* 806–817.
https://doi.org/10.3762/bjnano.17.57

Received: 10 December 2025
Accepted: 21 May 2026
Published: 17 June 2026

This article is part of the thematic issue "Sustainable nanomaterials for energy conversion and environmental remediation".

Associate Editor: C. T. Yavuz

© 2026 da Cunha et al.; licensee Beilstein-Institut.
License and terms: see end of document.

Abstract

The H_2 evolution from water electrolysis can be coupled with co-generation of other added-value products through biomass oxidation. In this study, we investigate the photoelectrochemical oxidation of glycerol using visible-light-responsive carbon nitride / bismuth vanadate (CN/$BiVO_4$) heterojunction photoelectrocatalysts. Different CN materials were explored, including polymeric carbon nitride (PCN), crystalline poly(heptazine imides) (PHI-Cat, in which Cat = Na, K, or Cs), and poly(triazine imide) (PTI-Li). The CN materials were spin-coated onto fluorine-doped tin oxide (FTO) substrates, followed by the Bi electrodeposition step and conversion to $BiVO_4$ in the presence of vanadyl acetylacetonate at 500 °C for 2 h. The CN/$BiVO_4$ heterojunctions presented bandgap energy values, E_g, similar to pure $BiVO_4$. X-ray diffraction analysis also revealed that the $BiVO_4$ phase was not altered by the presence of the CN. However, scanning electron microscopy analysis coupled to energy-dispersive X-ray spectroscopy (SEM-EDS) revealed regions rich in Bi and V, and others rich in C and N, suggesting the formation of heterojunctions. Photoelectrochemical studies demonstrated that $BiVO_4$ is active for both water and glycerol (1.0 mol·L^{-1}) oxidation, with a fourfold increase in photocurrent at 1.23 V vs reversible hydrogen electrode (RHE) upon glycerol addition. Clearly, the type of nitride employed in the heterojunctions influences the activity of the material for glycerol oxidation, with the photocurrent at 1.23 V vs RHE following the order: PCN/$BiVO_4$ > $BiVO_4$ ≈ PHI-Cs/$BiVO_4$ > PHI-K/$BiVO_4$ ≈ PHI-Na/$BiVO_4$ > PTI(Li)/$BiVO_4$. The SEM-EDS analysis after electrochemical tests revealed that the presence of crystalline CNs induces the segregation of vanadium oxides, contributing to a decrease in activity. On the other hand, the superior performance of PCN/$BiVO_4$ is attributed to a greater thermal stability of PCN during $BiVO_4$ synthesis, as indicated by thermogravimetric analysis. These findings highlight the dual importance of electronic compatibility and thermal resilience of CN materials in designing efficient heterojunction photoanodes for biomass-assisted hydrogen production.

Introduction

Hydrogen production based on sustainable and renewable energy sources (the so-called green-H_2) is a promising alternative for energy storage, with potential applications in fuel cells and the chemical industry [1]. Among the various methods of producing green-H_2 [2], water photoelectrolysis [3] allows the direct use of solar energy, decreasing reliance on fossil fuels, and having potential for large-scale hydrogen production [4]. On the other hand, the challenges related to the sluggish kinetics of the water oxidation reaction, as well as the material stability at the anodes, must be overcome for this technology to be successfully transferred to end users [5].

To address these issues, several efforts have been made to develop efficient catalysts to improve the kinetics of the water oxidation reaction [6]. These strategies include the synthesis of new photocatalysts, such as metal oxides, doped oxides, heterojunctions, and protective layers to enhance charge transfer at both interfaces and in the bulk, thereby lowering the activation energy barriers [7]. In this sense, bismuth vanadate ($BiVO_4$) has been pointed out as a promising material, as it presents high chemical stability and a wide absorption range of solar radiation [8-10]. To overcome the limitations associated with the low electrical conductivity of $BiVO_4$, sluggish surface kinetics and the recombination of electron–hole pairs [11], it is possible to combine $BiVO_4$ with other materials, such as carbon nitrides materials [12].

Carbon nitrides (CNs) can be classified into two main groups: polymeric carbon nitride (PCN) and crystalline carbon nitrides – poly(heptazine imide) (PHI) and poly(triazine imide) (PTI). While both share a fundamental heptazine or triazine-based backbone, they significantly differ in structure, crystallinity, and properties. PCN is the commonly synthesized form of CN due to its simple preparation methods. However, it suffers from low crystallinity, structural disorder, and poor reproducibility, which limit its performance in various applications [13,14]. In contrast, crystalline carbon nitrides, namely PHI and PTI, exhibit superior molecular organization, greater stability, and enhanced functional properties. PHI is composed of heptazine units linked through nitrogen bridges, resulting in a pseudo-hexagonal 2D lattice. Meanwhile, PTI consists of triazine units, forming a rigid and highly stable framework. This structural arrangement significantly improves charge mobility and light absorption, both of which are critical for catalytic activity [15]. Additionally, PHI and PTI possess an intrinsic ionic nature, unlike the neutral PCN, which enhances their interactions with various substrates and expands their potential applications. A key factor in achieving superior crystallinity of PHI and PTI is ionothermal synthesis, where the use of salts facilitates a well-ordered molecular arrangement and minimizes structural defects [16]. CN materials have been extensively studied as environmentally friendly semiconductors with remarkable photocatalytic properties and facile synthesis [17-21]. Furthermore, it has been demonstrated that incorporating cations during CN synthesis can lead to different structural modifications, varying degrees of crystallinity, and consequently, distinct photocatalytic performance [17-21].

Another strategy to bypass the sluggish kinetics of water oxidation involves employing different processes to deliver the electrons necessary for H_2 production. In this context, the oxidation of small organic molecules has great potential to replace water oxidation in photoelectrochemical cells [22], as these molecules have a considerably lower standard potential, with the possibility to yield value-added products. Indeed, biomass derivatives, such as ethanol and glycerol, are targeted to become a new route for converting solar energy into fuels [23] at both sides of the cells (i.e., while H_2 is produced at the cathode, carboxylic acids, aldehydes, and ketones can be produced at the anode [24]). It is expected that glycerol photoelectrochemical oxidation at $BiVO_4$ occurs by the following pathway: (i) Photon absorption by $BiVO_4$, (ii) electron–hole (e^-–h^+) separation, (iii) electron(s) transfer from glycerol molecule to h^+, and (iv) glycerol deprotonation yielding oxidized products as shown in Equation 1. The products usually described in the literature for this process are 1,3-dihydroxyacetone, glyceraldehyde, formic acid, and glyceric acid [25,26].

$$C_3H_8O_3 + nh^+ \rightarrow \text{Products} + nH^+ \quad (1)$$

Hessel et al. compared the photochemical oxidation of methanol, ethylene glycol, and glycerol in CdS [27], $BiVO_4$ [25], and $BiVO_4$:Zr,Mo/Pt [25] thin films, concluding that regardless of the material, glycerol oxidation depicted higher photocurrents and provided a protective effect against photocorrosion. The photoelectrochemical activity and selectivity of glycerol oxidation on $BiVO_4$ are influenced by several factors, including pH [26], electrolyte cation and anion [28], $BiVO_4$ surface crystallography orientation [29], and bismuth-rich domain within the film [30].

Herein, in order to understand the effect of distinct types of CN materials on CN/$BiVO_4$ heterojunctions, polymeric (PCN), poly(heptazine imide) (PHI) and poly(triazine imide) (PTI) carbon nitrides were synthesized and employed to fabricate CN/$BiVO_4$ electrodes. These heterojunctions were applied to photoelectrochemical glycerol oxidation. Furthermore, the effect of Na, K, and Cs alkaline cations in the PHI structures

was investigated and the photoactivity for glycerol oxidation was discussed in terms of CN thermal stability.

Materials and Methods

Synthesis of carbon nitrides

The PCN synthesis followed the procedure described by Silva et al. [31]. Briefly, the synthesis was carried out in a hydrothermal reactor for the polymerization of melamine in 25 mL of distilled water at 80 °C for 4 h. At the end of the process, the solvent was evaporated, and the resulting solid underwent thermal treatment at 550 °C for 30 min. The procedure described by Chen et al. [15] was adopted for PHI and PTI synthesis, in which melamine (1 g) was mixed with 10 g of alkali metal chlorides (Li, Na, K, or Cs), and the mixture was heated in a muffle furnace under a N_2 atmosphere. The heating conditions were adjusted based on the alkali metal chloride used: for Na, the system was heated at 600 °C for 4 h, for Li at 600 °C for 8 h, and for both K and Cs at 550 °C for 4 h. After heating, the product was washed with distilled water and stirred at 95 °C for 3 h. The suspension was then centrifuged at 9000 rpm for 5 min, dried in an oven at 60 °C, and stored for later use. While the synthesis containing LiCl results in the PTI structure, the other salts yield PHI [31,32].

Carbon nitride deposition onto FTO

An amount of 20 mg of each CN was dispersed into 5 mL of poly(ethylene glycol) (PEG-300, Sigma-Aldrich, ACS reagent, 99.99%) for 30 min in an ultrasound bath (Soni-tech ultrasonic cleaner). Subsequently, 60 µL of a freshly sonicated suspension was drop-cast onto a 1 × 1 cm FTO (Sigma-Aldrich, surface resistivity ≈7 Ω/sq) substrate cleaned/pre-treated according to the protocol described by Malviya et al. [31,32]. The system was spun at 2000 rpm for 30 s in a spin coater device (WS-650Hz-23NPPB). Finally, the C_3N_4/FTO layer was placed in a drying oven at a temperature of 300 °C for 1 h.

Synthesis of heterojunctions

Initially, bismuth was electrodeposited from a bismuth(III) nitrate (Sigma-Aldrich, ACS reagent, 99.99%) solution (0.02 mol·L^{-1} in ethylene glycol) by applying a −1.8 V vs Ag/AgCl/KCl_{sat} potential for five cycles (2 s at open circuit between the cycles) until reaching a charge density of −0.04 C·cm^{-2} at each cycle (total charge of −0.2 C·cm^{-2}) [33]. The electrodeposition was performed on both unmodified and FTO-modified subtrates with different CN. Subsequently, 60 µL of a vanadium(III) acetylacetonate (Sigma-Aldrich, ACS reagent, 99.99%) solution (0.2 mol·L^{-1} in DMSO) was drop-cast onto the freshly electrodeposited Bi layer, and the material was heated at 10 °C·min^{-1} up to 500 °C and held for 2 h. After completing this step, the films were soaked into NaOH solution (1.0 mol·L^{-1}) for 30 min to remove the excess of unreacted vanadium, washed with distilled water, and dried at ambient temperature.

Characterization of materials

Prior to deposition on FTO substrates, the different types of CN were structurally and morphologically characterized. Thermogravimetric (TGA) analysis (Netzsch, 209 F3) was performed from 25 to 800 °C at a heating rate of 10 °C·min^{-1} under a synthetic air atmosphere. X-ray diffraction (XRD) patterns (XRD, Rigaku Ultima IV 6000) were acquired from 10° to 80° at a rate of 2°·min^{-1} with a step size of 0.02°. Morphological features and elemental composition were determined by field-emission scanning electron microscopy (FEG-SEM; Zeiss Supra35) coupled with energy-dispersive X-ray spectroscopy (EDS), operating at 15 kV. Optical properties were investigated using ultraviolet–visible spectroscopy in the diffuse reflectance mode (Agilent-Cary Series UV–vis–NIR) in the wavelength range from 800 to 300 nm at 600 nm·min^{-1}. The optical energy band gap (E_g) values were estimated using the Kubelka–Munk function applied the Tauc equation (Supporting Information File 1, Equation S1) [34].

The photoelectrochemical characterization was carried out using a potentiostat/galvanostat (PGSTAT302N, Autolab, Metrohm). Measurements were performed in a three-electrode cell containing a Na_2SO_4 solution (0.5 mol·L^{-1}, pH 6.8), $BiVO_4$ or CN/$BiVO_4$ as working electrode (WE), a platinum sheet as the counter electrode, and a Ag/AgCl/KCl_{sat} electrode as potential reference. The light source was provided by solar simulator (Oriel, LCS-100, AM-1.5G) with 100 mW·cm^{-2} of irradiance illuminating the back side of the WE through a lateral quartz window in the electrochemical cell (Supporting Information File 1, Figure S1). Linear sweep voltammetry (LSV) curves were acquired in the dark and under simulated solar exposure, ranging from −0.6 to 1.4 V vs Ag/AgCl/KCl_{sat} at 50 mV·s^{-1}.

Results and Discussion

Physical characterization

The CNs thermostability was evaluated by TGA, as shown in Figure 1. PCN presented greater thermal stability at temperatures below 500 °C, the mass losses being more pronounced for temperatures higher than 550 °C, resulting in a residual mass of 3.3% at 700 °C. On the other hand, remaining materials (PTI-Li, PHI-Na, and PHI-K) exhibited mass losses at lower temperatures, which can be divided into two stages: (i) mass losses at T < 300 °C are probably due to water in the CN structures, which is connected to the residual water after the last part of the synthesis protocol which involves dissolution in water; (ii) mass losses at T > 300 °C are likely connected with the CN degradation, which happens at considerably lower temperatures than those observed for PCN. Interestingly, even at T = 800 °C in an

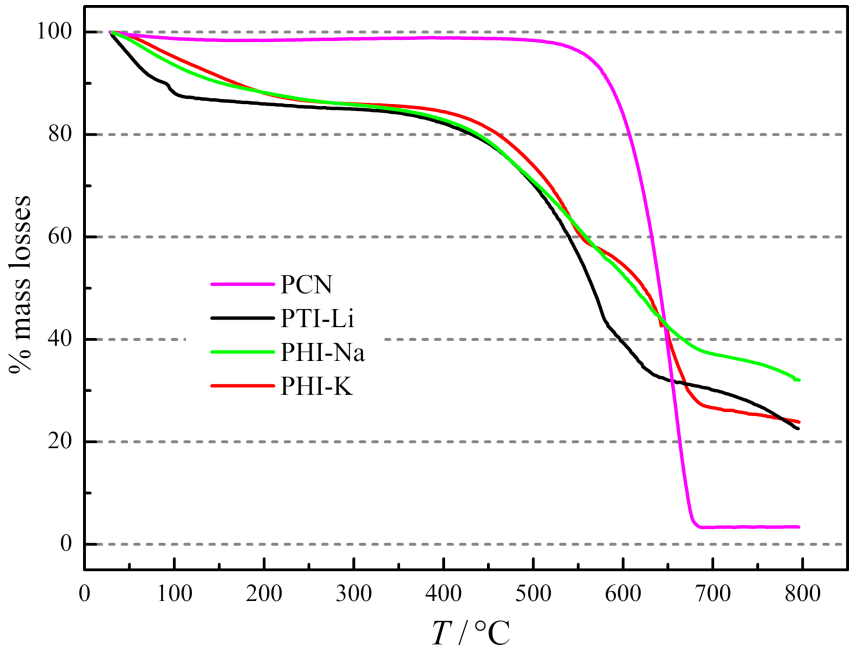


Figure 1: Thermogravimetric analysis of PCN, Li-PTI, Na-PHI, and K-PHI in synthetic air atmosphere.

oxidizing atmosphere, the materials still maintain 20–35% of their initial mass.

To shed some light on CN structure degradation and the residual nature of the materials at high temperature, a thermal treatment was performed at 500 °C for 2 h and the X-ray diffractograms were collected for the materials with the highest (PCN) and the lowest (PTI-Li) thermal stability. Supporting Information File 1, Figure S2 shows that PCN maintains the XRD pattern after the thermal treatment. On the other hand, PTI-Li suffers structural transformations during thermal treatment, resulting in a strong inhibition of the peaks at 11.8°, 21.2°, and 27.0° and the appearance of an intense and sharp peak at 31.8°. Supporting Information File 1, Figure S3 compares the PTI-Li XRD pattern with simulated XRD patterns of several lithium (hydro)oxides but it is not possible to address the observed features for only one species. Therefore, the material obtained after the thermal treatment seems to be a mixture of unreacted PCN with possibly lithium (hydro)oxides.

Figure 2 shows the XRD for the synthesized CNs/$BiVO_4$ films and for $BiVO_4$ and PCN films onto FTO substrate. The XRD pattern for clean FTO was also included (gray line) making it easier to observe its contribution to the other diffractograms. Notably, in all films, it is possible to observe the diffraction peaks related to the FTO (since the incident beam interacts with all layers of the material). The main FTO contributions are highlighted by the gray dashed lines. The film containing only $BiVO_4$ presents a diffraction pattern consistent with the monoclinic structure, according to ICDD file 00-044-0081. The following planes stand out, attested by the peaks that appear at 2θ = 18.7° (011), 28.7° (−121), 30.5° (004), 34.5° (200), 35.2° (202), 39.7° (211), 42.4° (105), and 47.1° (024) in agreement with the assignments reported by Cheng et al. [35]. These contributions are indicated by the red dashed lines. Furthermore, in films containing C_3N_4, it is not possible to observe its crystalline phase, likely due to the thin layer of this material on FTO. Supporting Information File 1, Figure S2 brings the CNs XRD for pristine powder forms in which the most intense peaks occur in the range from 26.8 to 28° for PTI-Li, PHI-Na, and PCN. Specifically, for PCN no peaks in this range are observed in Figure 2 for PCN onto FTO. Moreover, $BiVO_4$ depicts an intense peak in this region, hindering any possible PCN contribution in PCN/$BiVO_4$ XRD. Therefore, for the CNs/$BiVO_4$ films, both $BiVO_4$ and FTO characteristic diffraction peaks are observed, whereas for the PCN film on FTO only the characteristic FTO diffraction peaks are detected.

FEG-SEM images (Figure 3) were performed on the surface (top view) of the $BiVO_4$ and CN/$BiVO_4$ films. Globular structures characteristic of bismuth vanadate can be recognized along the surface, these patterns have been reported in the literature for $BiVO_4$ synthesized by similar procedures [25,33,36]. For the materials containing heterojunctions, the globular structures occurred in a different way for each material, which could be attributed to nucleation during the heat treatment, depending

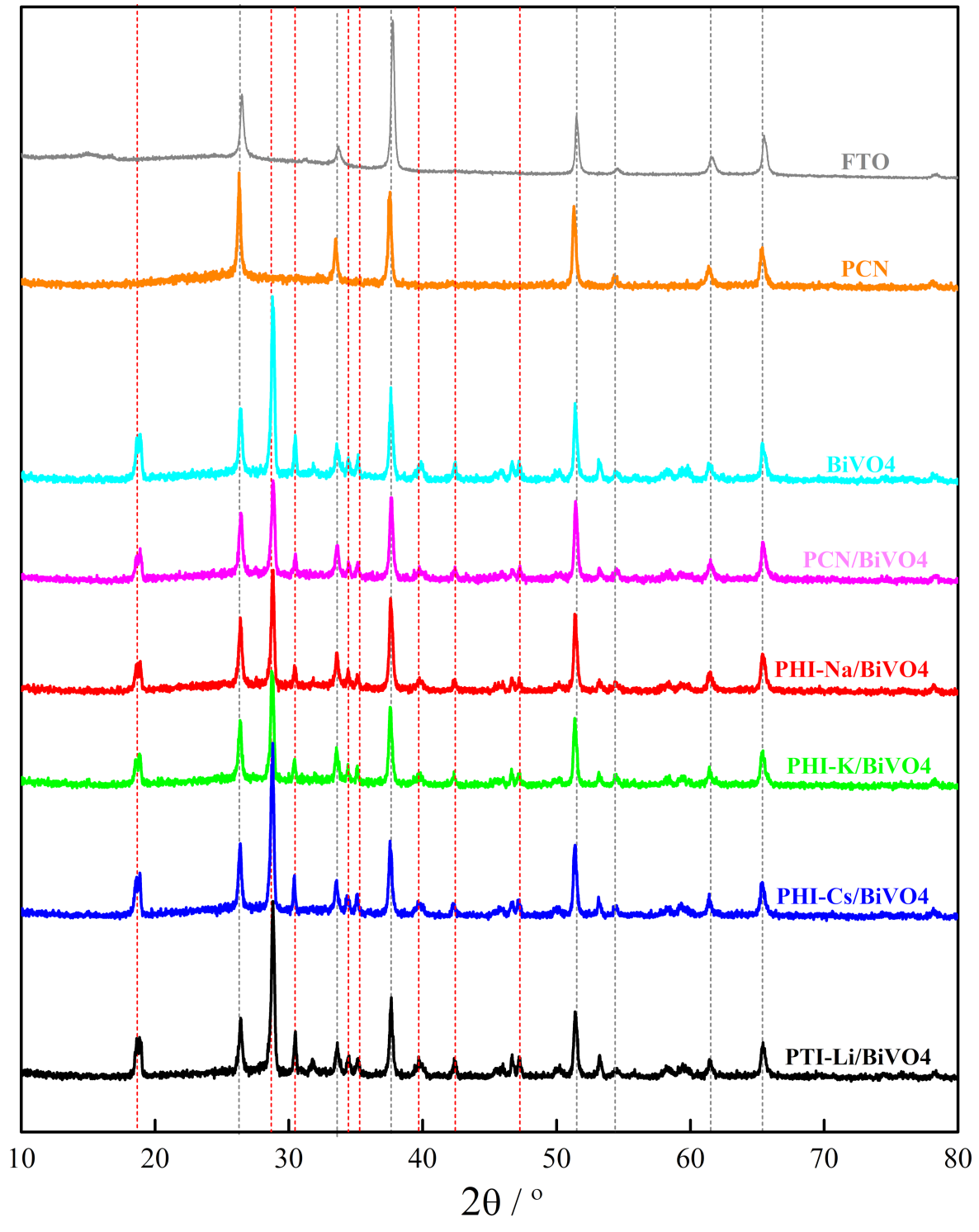


Figure 2: X-ray diffractograms for the material deposited onto FTO substrates.

on the alkali cation present or the CN crystallinity. For instance, in PCN/$BiVO_4$ and PHI-Na/$BiVO_4$ (Figure 3b and 3c), the globules decreased in size compared to pure $BiVO_4$, whereas in PHI-K/$BiVO_4$, PHI-Cs/$BiVO_4$, and PHI-Li/$BiVO_4$, they tended to agglomerate into elongated morphologies. SEM-EDS images for PHI-Li/$BiVO_4$ (Supporting Information File 1, Figure S4)

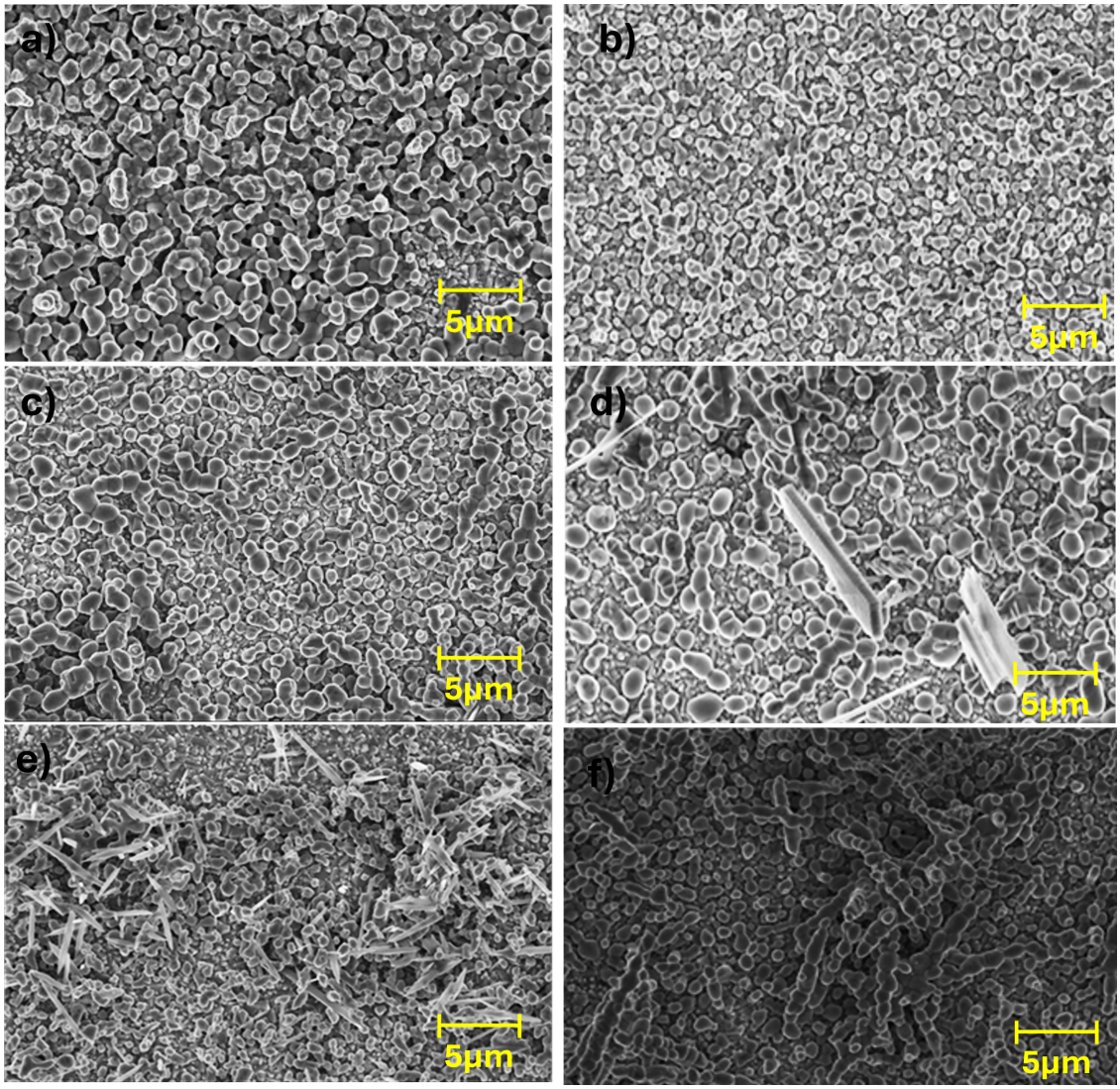


Figure 3: FEG-SEM images for a) $BiVO_4$; b) PCN/$BiVO_4$; c) PHI-Na/$BiVO_4$; d) PTI-Li/$BiVO_4$; e) PHI-K/$BiVO_4$; and f) PHI-Cs/$BiVO_4$ film onto FTO.

revealed that the elongated structures are richer in both vanadium and oxygen than in bismuth. Therefore, it can be concluded these structures are mainly vanadium oxides.

Cross-sectional FEG-SEM-EDS analysis was performed on PCN/$BiVO_4$ and PHI-Li/$BiVO_4$, (Figure 4) (i.e., the materials that showed the highest and lowest thermal stability, respectively). From the bottom to the top part of both samples, it is possible to recognize the following elements: Si from the glass support, Sn from the FTO layer, both C and N from the CN layer, and both Bi and V from the $BiVO_4$ layer. The C and N signals appear to be located in the same region as Sn, which can be interpreted as a thin CN layer distributed among the FTO grains. This is in agreement with the PCN/FTO FEG-SEM analysis (Supporting Information File 1, Figure S5) in which even after the PCN layer deposition, the typical FTO morphology is clearly observed. The Bi and V signals appear above the other elements, confirming that $BiVO_4$ is the species in contact with the electrolyte and suggesting the formation of a heterojunction. Finally, the scattered-colored dots in the images indicate that the analysis is near the detection limit of the instrument; therefore, the data should be qualitatively interpreted.

Figure 5 shows the Tauc plots derived from the diffuse reflectance spectra collected for the CN/$BiVO_4$ materials, assuming an indirect allowed transition. The bandgap energy values (E_g) were determined by the linear extrapolation of the linear region of the plots to the baseline. The E_g values were calculated in

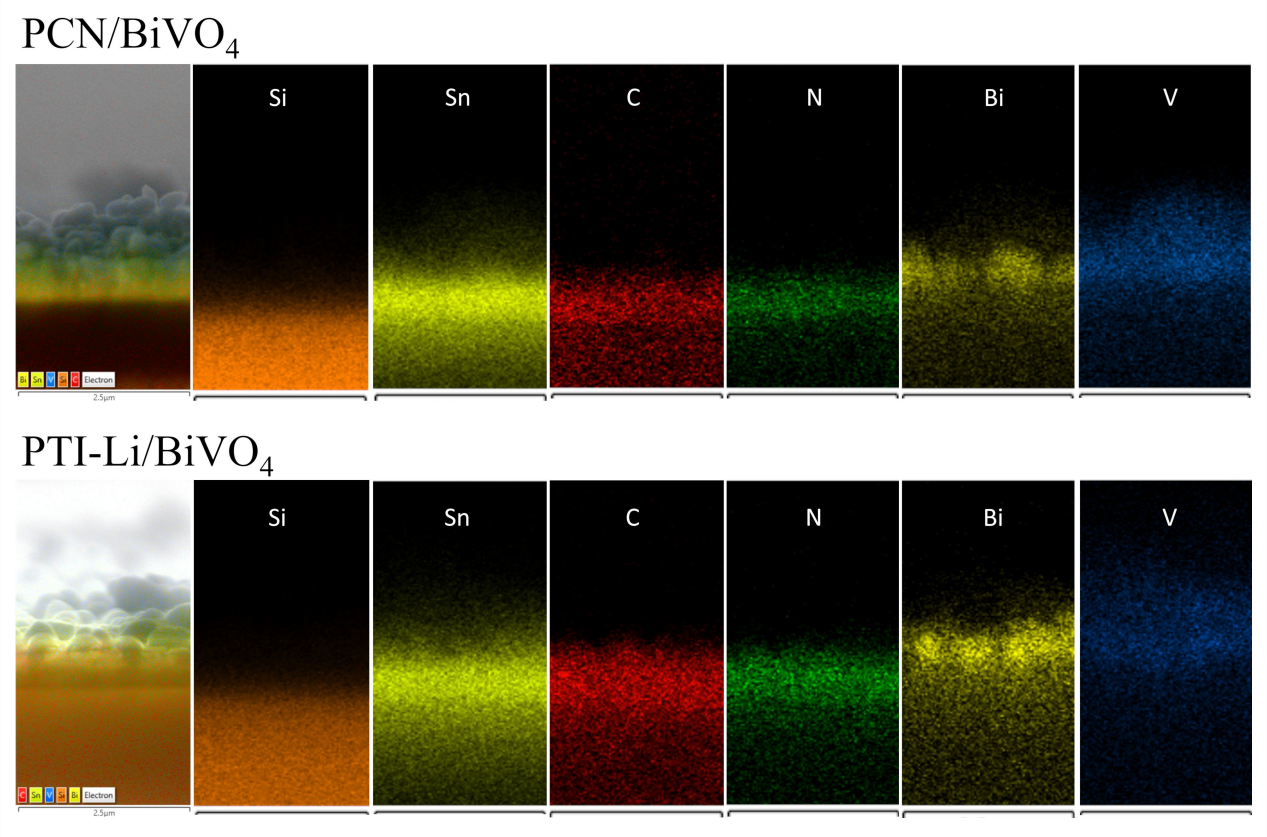


Figure 4: FEG-SEM-EDS images for PCN/$BiVO_4$ and PTI-Li/$BiVO_4$.

triplicate for each material, and the mean values, along with their standard deviations, are shown in Figure 5b. Overall, there are no significant variations among the materials, indicating that the underlying CN layer exerts little influence on the E_g of $BiVO_4$, which agrees with previous reports [37,38]. Furthermore, the E_g values for the CN samples in powder form were also determined. In this case, the E_g values are higher than those for CN/$BiVO_4$ films, as indicated by the blue triangles in Figure 5b, in agreement with the literature values [31].

Electrochemical characterization

Photoelectrochemical activities were evaluated by LSV at a scan rate of 0.05 $V{\cdot}s^{-1}$ in a Na_2SO_4 solution (0.5 $mol{\cdot}L^{-1}$, pH 6.8). Initially, the activity of the $BiVO_4$ film was investigated for water oxidation (in the supporting electrolyte alone) and subsequently for glycerol oxidation after the addition of 1.0 $mol{\cdot}L^{-1}$ glycerol (Figure 6a). Notably, in the presence of glycerol and simulated light (glycerol/on), the anodic photocurrent onset potential is negatively shifted by 300 mV and the photocurrent densities at 0.6 and 1.5 V are 4.3 and 1.5 times higher than those for water oxidation (water/on), respectively. The dotted lines also confirm that the material is inactive in the dark, regardless of the species in the electrolyte (water/off and glycerol/off).

Intermittent light measurements (chopped light) were also performed to evaluate the influence of pulsed light on the $BiVO_4$ photoactivity (Supporting Information File 1, Figures S6 and S7). In the presence of glycerol, the photocurrent closely follows the light on/off transitions, showing stable and sustained values under illumination. In contrast, under water oxidation conditions (i.e., in the absence of glycerol), a sharp current peak appears within fractions of a second upon illumination. These transient current peaks are related to the accumulation of holes (h^+) at the surface of the semiconductor, caused by the sluggish water oxidation kinetics [34].

Following the same protocol employed to test the $BiVO_4$, the photoelectrochemical activity of the CN/$BiVO_4$ films toward glycerol photoelectrochemical oxidation was also evaluated, and the results are displayed in Figure 6b. For comparison, the curve for the pristine $BiVO_4$ film was also included. Interestingly, the onset potential for glycerol oxidation does not depend on the CN type used on the heterojunction, suggesting no doping effect on $BiVO_4$. On the other hand, at higher applied potentials, the photocurrent density strongly depends on the CN type. The materials PTI-Li, PHI-Na, and PHI-K combined with $BiVO_4$ tend to decrease the overall activity for glycerol oxidation. In turn, PHI-Cs/$BiVO_4$ exhibits an activity similar to that

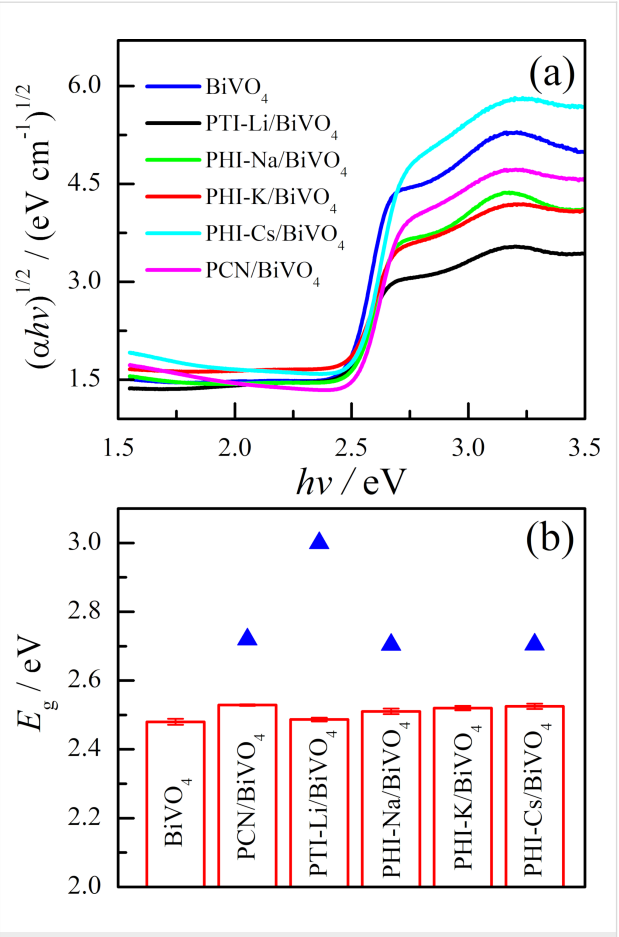


Figure 5: Tauc plot from UV–vis spectra (a) and bandgap energy for both $BiVO_4$ and CN/$BiVO_4$ films (b). The blue triangles represent the bandgap energy for the CN prior to FTO deposition.

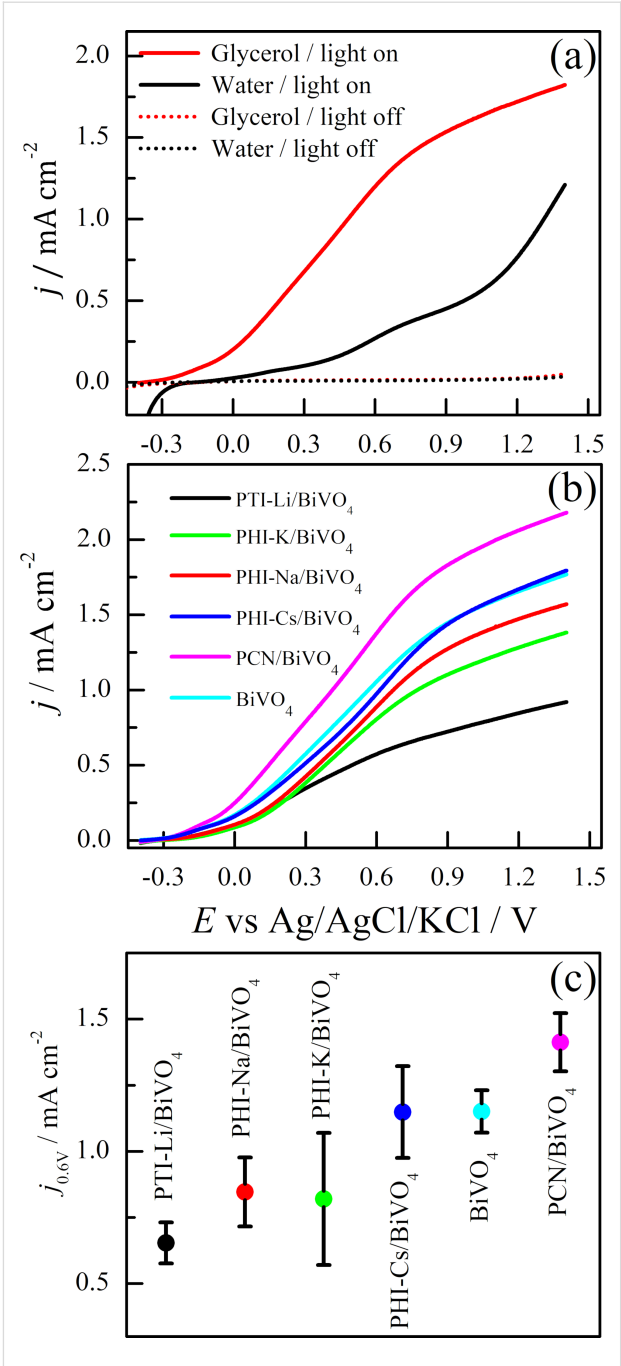


Figure 6: Comparison between photoelectrochemical oxidation of water and glycerol at the $BiVO_4$ photoanode under simulated solar illumination (light on) and dark (light off). (a) Glycerol photoelectrochemical oxidation at distinct CN-X/$BiVO_4$ films under simulated solar illumination. (b) Photocurrent mean values obtained in (b) at E = 0.6 V. (c) The error bars represent the standard deviations from three distinct independently produced films. Other conditions: electrolyte: Na_2SO_4 (0.5 mol·L^{-1}, pH 6.8) + glycerol (1.0 mol·L^{-1})v = 0.05 V·s^{-1}.

of bare $BiVO_4$, while PCN/$BiVO_4$ displays a higher activity. These photoelectrochemical tests were performed in triplicate using independently prepared electrodes, and the mean photocurrent densities at 0.6 V are shown in Figure 6b. Photocurrent densities under chopped illumination are also presented in Supporting Information File 1, Figures S8–S12 and follow the same trend observed under continuous irradiance. The PCN activity for glycerol was also tested (Supporting Information File 1, Figure S8b) in the same experimental conditions and released photocurrent of ca. 1 μA·cm^{-2}. Therefore, the positive effects observed on composite materials come from the synergy between $BiVO_4$ and CN.

Long-term electrolysis experiments were performed for PCN/$BiVO_4$ films at E = 0.6 V vs Ag/AgCl/KCl (1.23 V vs RHE) for 20 h under simulated solar illumination (Figure 7a). The photocurrent changes suggest that no corrosion effect or deactivation processes are occurring at the surface during glycerol oxidation. The inserts show FEG-SEM images of the surface before and after electrolysis, confirming that glycerol photoelectrochemical oxidation does not modify the surface condition. Finally, the Figure 7b brings the FEG-SEM-EDS elemental mapping before and after electrolysis. Comparing the images, all elements in pristine material are present after elec-

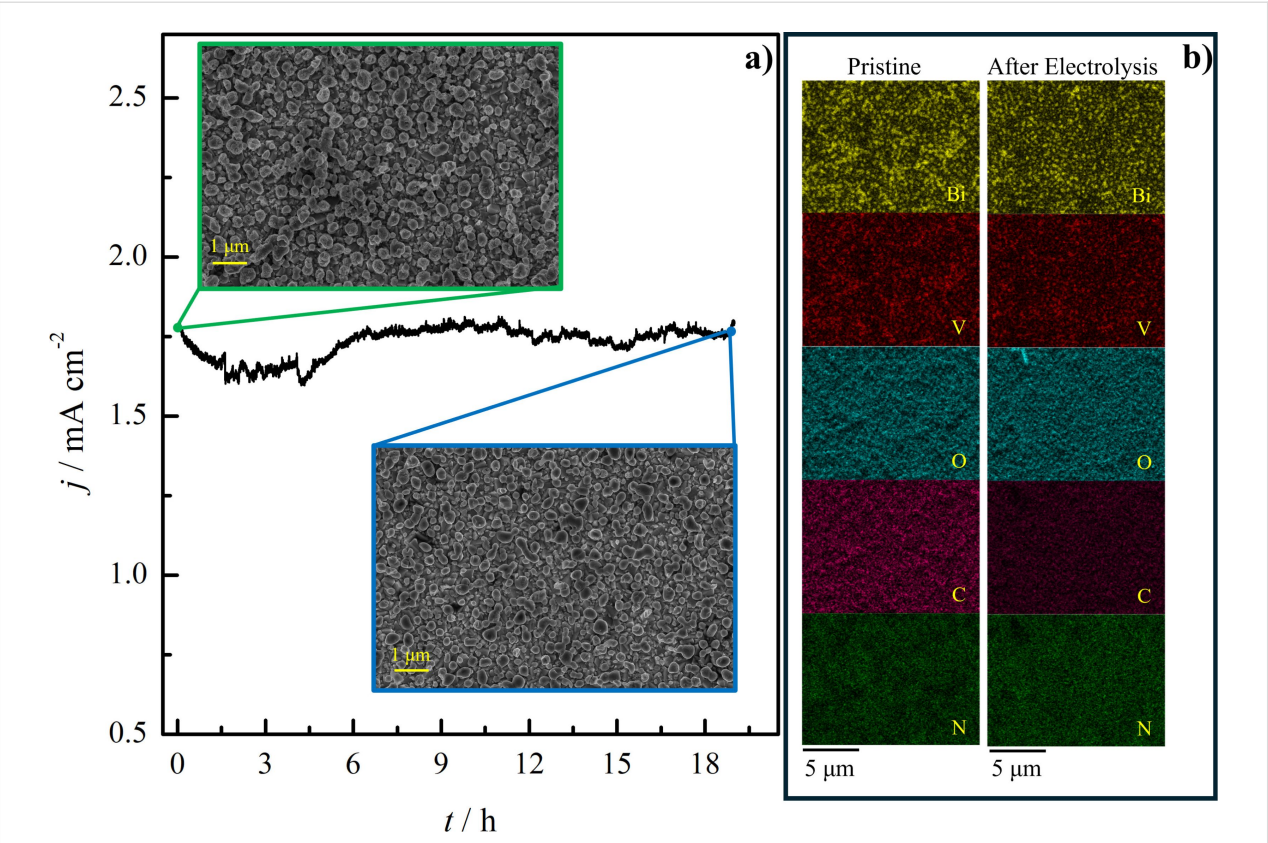


Figure 7: a) Current change at 0.6 V vs Ag/AgCl/KCl for 20 h under simulated solar illumination for PCN/$BiVO_4$ in Na_2SO_4 + glycerol. The inserts show the FEG-SEM images for pristine (t = 0) and post-electrolysis (20 h) electrode surface. b) Elemental analysis (FEG-SEM-EDS mapping) for the pristine and after-electrolysis electrode.

trolysis (i.e., it has not leached during electrolysis). Therefore, one can conclude the PCN/$BiVO_4$ is an active and stable material for glycerol photoelectrochemical oxidation.

During the $BiVO_4$ synthesis, an annealing step at 500 °C is necessary to obtain the monoclinic phase. Given the CNs thermal stabilities, significant structural changes are expected, as indicated by TGA analysis. The materials prepared with PTI-Li, PHI-Na, and PHI-K undergo substantial mass loss during this $BiVO_4$ synthesis step. In contrast, when coupled with $BiVO_4$, PCN, the most stable material among the CNs studied, exhibited a photocurrent density 22% higher than that of bare $BiVO_4$ for the glycerol oxidation at 0.6 V vs Ag/AgCl/KCl_{sat} (1.23 V vs RHE).

However, the inherent CNs thermal stability alone cannot explain the behavior of the entire set of tested materials. For instance, the FEG-SEM-EDS indicates the presence of both C and N under the $BiVO_4$ layer in the PCN/$BiVO_4$ and PTI-Li/$BiVO_4$ films. Therefore, a protective effect exerted by the Bi/$BiVO_4$ layer over the CNs could be enhancing the thermal stability of the underlying CNs during the $BiVO_4$ synthesis, thereby preventing mass loss. Indeed, thermal treatment of the bare CN films deposited onto FTO at 500 °C without the Bi overlayer leads to the complete thermal degradation of the CN layer. Furthermore, we also confirmed that the PTI-Li powder retains its original bandgap energy (E_g = 3.0 eV) after the thermal treatment at 500 °C for 2 h (Supporting Information File 1, Figure S13).

The films composed of PHI-K/$BiVO_4$ and PHI-Cs/$BiVO_4$ exhibit activities similar to pristine $BiVO_4$, but the thermal stability of PHI-K/$BiVO_4$ is comparable to that of PTI-Li. The literature suggests that the crystallinity of PHI structures increases as the cation radius decreases. This means that PHI synthesized in the presence of smaller cations, such as Na^+, exhibits a higher degree of crystallinity compared to those prepared with larger cations, such as K^+. This trend can be attributed to the stronger electrostatic interactions and more efficient packing of smaller cations within the negatively charged imide-linked framework. Smaller cations fit more compactly within the pores and interlayer spaces, promoting a more ordered and rigid structural arrangement. In contrast, larger cations, such as K^+, create greater spatial distortions, leading to reduced crystallinity and a

less well-defined long-range order [15,16,39]. Although it was not possible to confirm these CN structural features by XRD analysis, the photoactivity toward glycerol oxidation follows this trend. In this scenario, the dependence of photoactivity with the CN type could arise from the charge transfer dynamics within the CN layer or at the interface between CN and $BiVO_4$, both of which can be tuned by the CN crystalline structure.

Considering that the E_g values observed for pristine CNs are maintained after thermal treatment under the Bi layer, the low photoactivity for glycerol oxidation at the PTI-Li/$BiVO_4$ film could be explained by the high E_g of PTI-Li, which likely hinders proper band alignment with $BiVO_4$. Both PHI-Na and PHI-Cs exhibited similar E_g values to that of PCN; however, the higher photoactivity of PCN/$BiVO_4$ likely arises from its superior thermal stability or more favorable band position. Furthermore, it is possible that the CNs thermally treated under Bi/$BiVO_4$ layer exhibit distinct features from those observed for the pristine materials. Unfortunately, techniques such as XRD and Mott–Schottky measurements, typically employed to estimate the crystalline phase and flat band potential, respectively, are challenging to perform on these CN layers with the features of those thermally treated under the Bi layer.

Interestingly, the higher activity observed for glycerol oxidation in PCN/$BiVO_4$ is consistent with Gonzaga et al. [12], who reported enhanced $BiVO_4$ activity when combined with PCN for textile wastewater detoxification. Thus, coupling $BiVO_4$ with PCN appears to be an effective strategy to boost the photocurrent in $BiVO_4$-based systems for the oxidation of organic molecules.

Conclusion

CN/$BiVO_4$ heterojunctions were successfully synthesized and characterized using UV–vis spectroscopy, SEM-EDS, XRD, and TGA. These materials were applied to the photoelectrochemical oxidation of glycerol, with particular attention given to the impact of thermal stability. Compared to bare $BiVO_4$, heterojunctions based on PTI-Li, PHI-Na, and PHI-K exhibited reduced photoactivity for glycerol oxidation, while PHI-Cs/$BiVO_4$ showed comparable performance. Notably, the PCN/$BiVO_4$ heterojunction demonstrated enhanced photoelectrochemical activity relative to that of $BiVO_4$ alone.

These results highlight the critical role of the CN component in determining the overall performance of the heterojunction. Beyond intrinsic electronic properties, factors such as the nature of the alkali cations, synthesis method, and post-synthesis thermal treatments significantly influence the structural integrity and interfacial behavior of CN materials. Therefore, the design of efficient CN-based heterojunctions must consider not only the initial properties of the CN but also how these properties evolve under processing conditions relevant to device fabrication and operation.

Supporting Information

Supporting Information File 1

Additional figures.
[https://www.beilstein-journals.org/bjnano/content/supplementary/2190-4286-17-57-S1.pdf]

Acknowledgements

The authors thank Shell for the strategic importance of the support given by ANP (Brazil's National Oil, Natural Gas, and Biofuels Agency) through the R&D levy regulation.

Funding

This research was funded by Fundação de Amparo a Pesquisa do Estado de São Paulo, FAPESP, grant numbers #2017/11986-5, #2024/06318-7, #2020/14741-6, #2021/11162-8, #2024/00839-5, #2024/20757-3 and #2021/12394-0, the Conselho Nacional de Desenvolvimento Científico e Tecnológico, CNPq, grant numbers #403064/2021, #310550/2022-0, and #405752/2022, Financiadora de Estudos e Projetos (FINEP) grant numbers #01.22.0179.00, 01.23.0645.00, and 01.23.0662.00.

Author Contributions

Charles Garcia da Cunha: conceptualization; data curation; formal analysis; investigation; methodology; writing – original draft. Isabelle M. D. Gonzaga: conceptualization; data curation; formal analysis; investigation; methodology; writing – original draft. Cristian Hessel: formal analysis; investigation; methodology; writing – original draft. Izadora F. Reis: formal analysis; investigation; methodology; writing – original draft. Ivo F. Teixeira: conceptualization; writing – original draft; writing – review & editing. Lucia H. Mascaro: conceptualization; writing – original draft; writing – review & editing. Elton Sitta: conceptualization; formal analysis; funding acquisition; methodology; supervision; writing – original draft; writing – review & editing.

ORCID® iDs

Charles Garcia da Cunha - https://orcid.org/0009-0002-8837-3989
Isabelle M. D. Gonzaga - https://orcid.org/0000-0001-8117-0295
Ivo F. Teixeira - https://orcid.org/0000-0002-4356-061X
Elton Sitta - https://orcid.org/0000-0003-3181-0076

Data Availability Statement

All data that supports the findings of this study is available in the published article and/or the supporting information of this article.

References

1. Amini Horri, B.; Ozcan, H. *Curr. Opin. Green Sustainable Chem.* **2024,** *47,* 100932. doi:10.1016/j.cogsc.2024.100932
2. Zainal, B. S.; Ker, P. J.; Mohamed, H.; Ong, H. C.; Fattah, I. M. R.; Rahman, S. M. A.; Nghiem, L. D.; Mahlia, T. M. I. *Renewable Sustainable Energy Rev.* **2024,** *189,* 113941. doi:10.1016/j.rser.2023.113941
3. Khan, D. A.; Choudhary, A. K.; Sharma, D. *Hydrogen Energy;* CRC Press: Boca Raton, 2024. doi:10.1201/9781003537816
4. Maggio, G.; Vasta, S.; Nicita, A.; Trocino, S.; Giorgianni, M. *Energies (Basel, Switz.)* **2025,** *18,* 1439. doi:10.3390/en18061439
5. Inocêncio, C. V. M.; Holade, Y.; Morais, C.; Kokoh, K. B.; Napporn, T. W. *Electrochem. Sci. Adv.* **2023,** *3,* e2100206. doi:10.1002/elsa.202100206
6. El ouardi, M.; El Idrissi, A.; Arab, M.; Zbair, M.; Haspel, H.; Saadi, M.; Ait Ahsaine, H. *Int. J. Hydrogen Energy* **2024,** *51,* 1044–1067. doi:10.1016/j.ijhydene.2023.09.111
7. Chen, T.-W.; Ramachandran, R.; Chen, S.-M.; Anushya, G.; Al-Sehemi, A. G.; Mariyappan, V.; Alargarsamy, S.; Alam, M. M.; Mahesh, T. C.; Kalimuthu, P.; Kannan, R. *Int. J. Electrochem. Sci.* **2024,** *19,* 100542. doi:10.1016/j.ijoes.2024.100542
8. Corradini, P. G.; de Brito, J. F.; Blaskievicz, S. F.; Salvati, B. S.; Menezes, B. C. e. S.; Zanoni, M. V. B.; Mascaro, L. H. *J. Photochem. Photobiol., A* **2023,** *444,* 114901. doi:10.1016/j.jphotochem.2023.114901
9. Lu, G.; Lun, Z.; Liang, H.; Wang, H.; Li, Z.; Ma, W. *J. Alloys Compd.* **2019,** *772,* 122–131. doi:10.1016/j.jallcom.2018.09.064
10. Orimolade, B. O.; Arotiba, O. A. *J. Electroanal. Chem.* **2020,** *878,* 114724. doi:10.1016/j.jelechem.2020.114724
11. Xie, Z.; Chen, D.; Zhai, J.; Huang, Y.; Ji, H. *Appl. Catal., B* **2023,** *334,* 122865. doi:10.1016/j.apcatb.2023.122865
12. Gonzaga, I. M. D.; Gonçalves, R.; Fernandes, C. H. M.; Assis, M.; Teixeira, I. F.; Mascaro, L. H. *Chemosphere* **2024,** *352,* 141315. doi:10.1016/j.chemosphere.2024.141315
13. Schlomberg, H.; Kröger, J.; Savasci, G.; Terban, M. W.; Bette, S.; Moudrakovski, I.; Duppel, V.; Podjaski, F.; Siegel, R.; Senker, J.; Dinnebier, R. E.; Ochsenfeld, C.; Lotsch, B. V. *Chem. Mater.* **2019,** *31,* 7478–7486. doi:10.1021/acs.chemmater.9b02199
14. Bojdys, M. J.; Müller, J.-O.; Antonietti, M.; Thomas, A. *Chem. – Eur. J.* **2008,** *14,* 8177–8182. doi:10.1002/chem.200800190
15. Chen, Z.; Savateev, A.; Pronkin, S.; Papaefthimiou, V.; Wolff, C.; Willinger, M. G.; Willinger, E.; Neher, D.; Antonietti, M.; Dontsova, D. *Adv. Mater. (Weinheim, Ger.)* **2017,** *29,* 1700555. doi:10.1002/adma.201700555
16. Dontsova, D.; Pronkin, S.; Wehle, M.; Chen, Z.; Fettkenhauer, C.; Clavel, G.; Antonietti, M. *Chem. Mater.* **2015,** *27,* 5170–5179. doi:10.1021/acs.chemmater.5b00812
17. Cao, S.; Low, J.; Yu, J.; Jaroniec, M. *Adv. Mater. (Weinheim, Ger.)* **2015,** *27,* 2150–2176. doi:10.1002/adma.201500033
18. Ansari, S. A.; Ansari, M. O.; Cho, M. H. *Sci. Rep.* **2016,** *6,* 27713. doi:10.1038/srep27713
19. da Silva, M. A. R.; Rocha, G. F. S. R.; Diab, G. A. A.; Cunha, C. S.; Pastana, V. G. S.; Teixeira, I. F. *Chem. Eng. J.* **2023,** *460,* 141068. doi:10.1016/j.cej.2022.141068
20. Huang, Y.-C.; Chen, J.; Lu, Y.-R.; Arul, K. T.; Ohigashi, T.; Chen, J.-L.; Chen, C.-L.; Shen, S.; Chou, W.-C.; Pong, W.-F.; Dong, C.-L. *J. Electron Spectrosc. Relat. Phenom.* **2023,** *264,* 147319. doi:10.1016/j.elspec.2023.147319
21. Blaskievicz, S. F.; Teixeira, I. F.; Mascaro, L. H. *J. Solid State Electrochem.* **2025,** *29,* 1025–1034. doi:10.1007/s10008-024-06029-8
22. Yang, S.; Yang, J.; Duan, M.; Kang, S.; He, S.; Chen, C. *Trans. Tianjin Univ.* **2024,** *30,* 167–177. doi:10.1007/s12209-024-00387-0
23. Sun, Y.; Miao, J.; Fan, X.; Zhang, K.; Zhang, T. *Small Struct.* **2024,** *5,* 2300576. doi:10.1002/sstr.202300576
24. Miao, Y.; Li, Z.; Shao, M. *ChemCatChem* **2024,** *16,* e202301321. doi:10.1002/cctc.202301321
25. Hessel, C.; Moreti, L.; Yukuhiro, V. Y.; Fernández, P. S.; Sitta, E. *Electrochim. Acta* **2025,** *509,* 145300. doi:10.1016/j.electacta.2024.145300
26. Liu, D.; Liu, J.-C.; Cai, W.; Ma, J.; Yang, H. B.; Xiao, H.; Li, J.; Xiong, Y.; Huang, Y.; Liu, B. *Nat. Commun.* **2019,** *10,* 1779. doi:10.1038/s41467-019-09788-5
27. Hessel, C.; Perini, N.; Sitta, E. *J. Solid State Electrochem.* **2023,** *27,* 705–714. doi:10.1007/s10008-022-05363-z
28. Kong, H.; Gupta, S.; Pérez-Torres, A. F.; Höhn, C.; Bogdanoff, P.; Mayer, M. T.; van de Krol, R.; Favaro, M.; Abdi, F. F. *Chem. Sci.* **2024,** *15,* 10425–10435. doi:10.1039/d4sc01651c
29. Vo, T.-G.; Kao, C.-C.; Kuo, J.-L.; Chiu, C.-c.; Chiang, C.-Y. *Appl. Catal., B* **2020,** *278,* 119303. doi:10.1016/j.apcatb.2020.119303
30. Lu, Y.; Lee, B. G.; Lin, C.; Liu, T.-K.; Wang, Z.; Miao, J.; Oh, S. H.; Kim, K. C.; Zhang, K.; Park, J. H. *Nat. Commun.* **2024,** *15,* 5475. doi:10.1038/s41467-024-49662-7
31. Silva, I. F.; Teixeira, I. F.; Rios, R. D. F.; do Nascimento, G. M.; Binatti, I.; Victória, H. F. V.; Krambrock, K.; Cury, L. A.; Teixeira, A. P. C.; Stumpf, H. O. *J. Hazard. Mater.* **2021,** *401,* 123713. doi:10.1016/j.jhazmat.2020.123713
32. Savateev, A.; Pronkin, S.; Willinger, M. G.; Antonietti, M.; Dontsova, D. *Chem. – Asian J.* **2017,** *12,* 1517–1522. doi:10.1002/asia.201700209
33. Shaddad, M. N.; Hezam, M.; Arunachalam, P.; AL-Saeedan, N. M.; Gimenez, S.; Bisquert, J.; Al-Mayouf, A. M. *Mater. Lett.* **2022,** *325,* 132799. doi:10.1016/j.matlet.2022.132799
34. Chen, Z.; Dinh, H. N.; Miller, E. *Photoelectrochemical Water Splitting;* Springer Briefs in Energy; Springer New York: New York, NY, 2013. doi:10.1007/978-1-4614-8298-7
35. Cheng, B.; Wang, W.; Shi, L.; Zhang, J.; Ran, J.; Yu, H. *Int. J. Photoenergy* **2012,** *2012,* 797968. doi:10.1155/2012/797968
36. Coelho, D.; Gaudêncio, J. P. R. S.; Carminati, S. A.; Ribeiro, F. W. P.; Nogueira, A. F.; Mascaro, L. H. *Chem. Eng. J.* **2020,** *399,* 125836. doi:10.1016/j.cej.2020.125836
37. Starukh, H.; Praus, P. *Catalysts* **2020,** *10,* 1119. doi:10.3390/catal10101119
38. Pingmuang, K.; Chen, J.; Kangwansupamonkon, W.; Wallace, G. G.; Phanichphant, S.; Nattestad, A. *Sci. Rep.* **2017,** *7,* 8929. doi:10.1038/s41598-017-09514-5
39. Savateev, A.; Dontsova, D.; Kurpil, B.; Antonietti, M. *J. Catal.* **2017,** *350,* 203–211. doi:10.1016/j.jcat.2017.02.029

License and Terms

This is an open access article licensed under the terms of the Beilstein-Institut Open Access License Agreement (https://www.beilstein-journals.org/bjnano/terms), which is identical to the Creative Commons Attribution 4.0 International License (https://creativecommons.org/licenses/by/4.0). The reuse of material under this license requires that the author(s), source and license are credited. Third-party material in this article could be subject to other licenses (typically indicated in the credit line), and in this case, users are required to obtain permission from the license holder to reuse the material.

The definitive version of this article is the electronic one which can be found at:
https://doi.org/10.3762/bjnano.17.57

BEILSTEIN JOURNAL OF NANOTECHNOLOGY

Light-driven ammonia electrooxidation via carbon nitride–ruthenium molecular interfaces

Jan Holub*[1] and Pablo Jiménez-Calvo*[2,3,4]

Perspective

Open Access

Address:
[1]Group of Coordination Chemistry, University of Chemistry and Technology, Prague (UCT, Prague); Department of Inorganic Chemistry, Technická 5, 166 28, Prague, Czech Republic, [2]Chemistry of Thin Film Materials, Materials Chemistry Section, Friedrich-Alexander-Universität Erlangen-Nürnberg, Cauerstraße 3, IZNF, Erlangen 91058, Germany, [3]Friedrich-Alexander-Universität Erlangen-Nürnberg, Profile Center Solar (FAU Solar), Freyeslebenstraße 1, 91058 Erlangen, Germany and [4]Department of Colloid Chemistry, Max-Planck-Institute of Colloids and Interfaces, Am Mühlenberg 1, 14476 Potsdam, Germany

Email:
Jan Holub* - holubj@vscht.cz; Pablo Jiménez-Calvo* - pablo.jimenez.calvo@fau.de

* Corresponding author

Keywords:
ammonia oxidation; carbon nitride; hybrid semiconductor–molecular interfaces; molecular ruthenium catalysts; photoelectrocatalysis

Beilstein J. Nanotechnol. **2026,** *17,* 854–862.
https://doi.org/10.3762/bjnano.17.61

Received: 11 April 2026
Accepted: 16 June 2026
Published: 08 July 2026

This article is part of the thematic issue "Sustainable nanomaterials for energy conversion and environmental remediation".

Associate Editor: J. J. Schneider

© 2026 Holub and Jiménez-Calvo; licensee Beilstein-Institut.
License and terms: see end of document.

Abstract

The homogeneous–heterogeneous catalysis gap remains an unresolved challenge in solar fuels research. Molecular catalysts offer unique selectivity and mechanistic transparency but suffer from poor electrode contact and limited recyclability, while heterogeneous semiconductors provide scalable light harvesting but lack precisely defined active sites. Anchoring molecular ruthenium (Ru) catalysts onto heterogeneous semiconductors, like carbon nitride (C_3N_4), offers a chemically rational strategy to bridge this gap, yielding hybrid photoelectrodes capable of driving ammonia oxidation, a reaction of growing importance as a sustainable hydrogen carrier. Inspired by natural photosynthesis, in which a light-harvesting antenna is spatially coupled to a multielectron catalytic centre, the proposed hybrid system assigns distinct and complementary roles to each component: C_3N_4 absorbs visible light, separates charge carriers, and provides a structurally tunable aromatic surface, while the metal complexes, e.g., RuBda, RuTda, or RuTpyBpy, accept photogenerated holes and drive the demanding six-electron oxidation of ammonia through well-defined coordination chemistry. Two anchoring strategies, covalent amide bond formation exploiting the surface amine groups of C_3N_4, and non-covalent π–π and C–H···π interactions mediated by pyrene-functionalized ligands, are presented as complementary rather than competing routes to the heterointerface, each controlling surface density, electronic coupling, and catalyst stability differently. This perspective article examines how the structural diversity of the C_3N_4 allotropes, spanning semicrystalline polymeric C_3N_4, highly ordered poly(heptazine imide), and high-surface-area amorphous sulfur-doped C_3N_4, offers a tunable platform for optimizing charge carrier dynamics at the hybrid interface. Finally, photoelectrocatalysis is the enabling configuration: Simultaneous illumina-

tion and electrochemical bias reduce the thermodynamic penalty, suppress charge recombination, and provide independent control over product selectivity. Despite available materials, precedent reactions, and compelling mechanistic rationale, no study to date has reported photoelectrocatalytic ammonia oxidation at a C_3N_4–Ru hybrid photoelectrode, this gap is the motivation and the central argument of this perspective.

Perspective

A) The energy challenge and the catalysis gap

The global transition away from fossil fuels demands new paradigms for how chemical energy is stored and released. At the heart of this challenge lies catalysis. For decades, it has been divided into two families, yet their integration is already bearing fruit. In water oxidation catalysis, molecular-semiconductor hybrids have demonstrated performance in electrocatalytic and photocatalytic systems, as proof of concept for bridging homogeneous precision with heterogeneous scalability. Homogeneous catalysts (molecular complexes in solution) operate with exquisite precision, that is, well-defined active sites, traceable mechanisms, and selective tunability achievable atom by atom via ligand design. Heterogeneous catalysts (metal oxides, nanoparticles, and carbon supports) are manufactured into electrodes or serve as the electrode itself, industrially scalable, but with poorly understood active sites and inactive bulk material [1-5].

In practice, however, bridging these two families is not straightforward. A homogeneous catalyst dissolved in solution faces a fundamental limitation: Only a tiny fraction of dissolved molecules is ever close enough to an electrode surface to participate in electron transfer at any given moment. The rest drifts idly in solution, increasing precious metal loading without contributing to the reaction. Heterogeneous catalysts solve the electrode contact problem but introduce their own: In a thick particle film, only the outermost surface layer is electrochemically accessible, while the underlying bulk is not [6,7]. For reactions that require both a light-absorbing semiconductor and a chemically active catalytic centre, as is the case in solar fuel production, neither paradigm alone is sufficient. What is needed is a hybrid architecture that positions a well-defined molecular catalyst directly at the surface of a photoactive solid, combining the selectivity of homogeneous catalysis with the processability and light-harvesting capacity of heterogeneous materials [1-5,8].

This perspective focuses on the well-known combination regarding water oxidation, that is, C_3N_4 semiconductors with molecular Ru-based catalysts as one promising multicomposite hybrid strategy. C_3N_4 acts as the light absorber and charge-conducting scaffold, functionally analogous to a photosensitizer, while the Ru complex serves as the molecular catalytic centre and light absorber too. Transferring this synergistic photoactive interface concept into photoelectrocatalysis for ammonia oxidation, a sustainable hydrogen carrier, remains an open and compelling opportunity [8].

B) Learning from nature: photosynthesis as the conceptual template

The photoactive system took inspiration from natural photosynthesis (Figure 1). Plants, algae, and cyanobacteria optimise the conversion of sunlight into chemical energy, and the architecture they arrived at contains design principles of elegance that chemists are only beginning to replicate [9]. In the thylakoid membrane of plant chloroplasts, light harvesting begins with antenna complexes, assemblies of pigment molecules, chlorophylls and carotenoids, arranged in a precisely ordered protein scaffold. These antenna pigments absorb photons across a broad range of the visible spectrum and funnel the resulting electronic excitation energy, with near-unity quantum efficiency, to a specialised reaction centre. This energy funnelling process is called photosensitization: The antenna molecules do not themselves drive the chemistry, but they extend the spectral range and photon capture cross section of the system, ensuring that the reaction centre receives a concentrated supply of excitation energy even under low-light conditions [9,10].

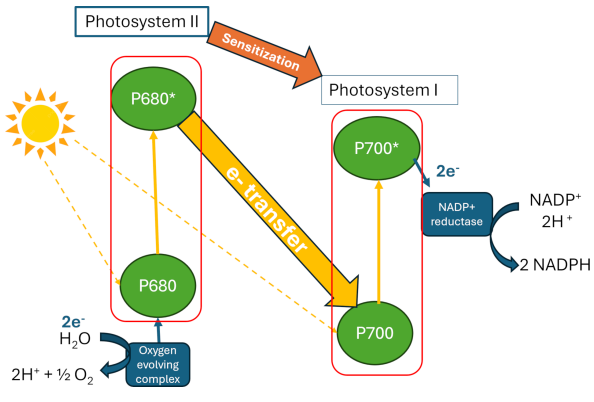


Figure 1: Scheme of photosynthesis, focusing on the electron transfer and the sensitisation effect.

At the reaction centre of Photosystem II, the absorbed excitation drives the oxidation of water (a thermodynamically demanding four-electron, four-proton process) at an inorganic cluster containing four manganese ions and one calcium ion (Mn_4CaO_5). The electrons extracted from water are passed along the electron transport chain to Photosystem I, where they reduce biological reductant $NADP^+$ to NADPH, which powers carbon fixation. The protons liberated by water oxidation are used to drive ATP synthesis, and the oxygen released is the molecular oxygen that constitutes Earth's atmosphere. The entire system is spatially organised within the membrane so that charge separation is maintained over nanometer distances and millisecond timescales, preventing the wasteful back-recombination of electrons and holes, which is the principal enemy of artificial photochemical systems [9,10].

Two lessons from this biological blueprint are instructive for materials design. First, the photosensitization principle: Light harvesting and catalytic chemistry are performed by distinct, spatially separated components that are electronically coupled at their interface. The antenna extends the absorption, the reaction centre does the chemistry. Second, the spatial organisation principle: Efficient photochemistry requires the light-generated charge carriers to be separated at an interface and driven to specific catalytic sites before they recombine. Achieving these two principles in a synthetic, scalable, and inexpensive material is the central aspiration, if not the "holy grail" of artificial photosynthesis.

In artificial photoelectrocatalytic systems, light-driven reactions follow five sequential steps (Figure 2a): (1) Photon absorption by the semiconductor generates a bound electron–hole pair, or exciton; (2) the exciton undergoes dissociation into spatially separated free charge carriers, a thermally and field-assisted step driven by the intrinsic electric field at the semiconductor–electrolyte junction; (3) the resulting free electrons populate the conduction band, while holes remain in the valence band; (4) carriers diffuse through the bulk toward the

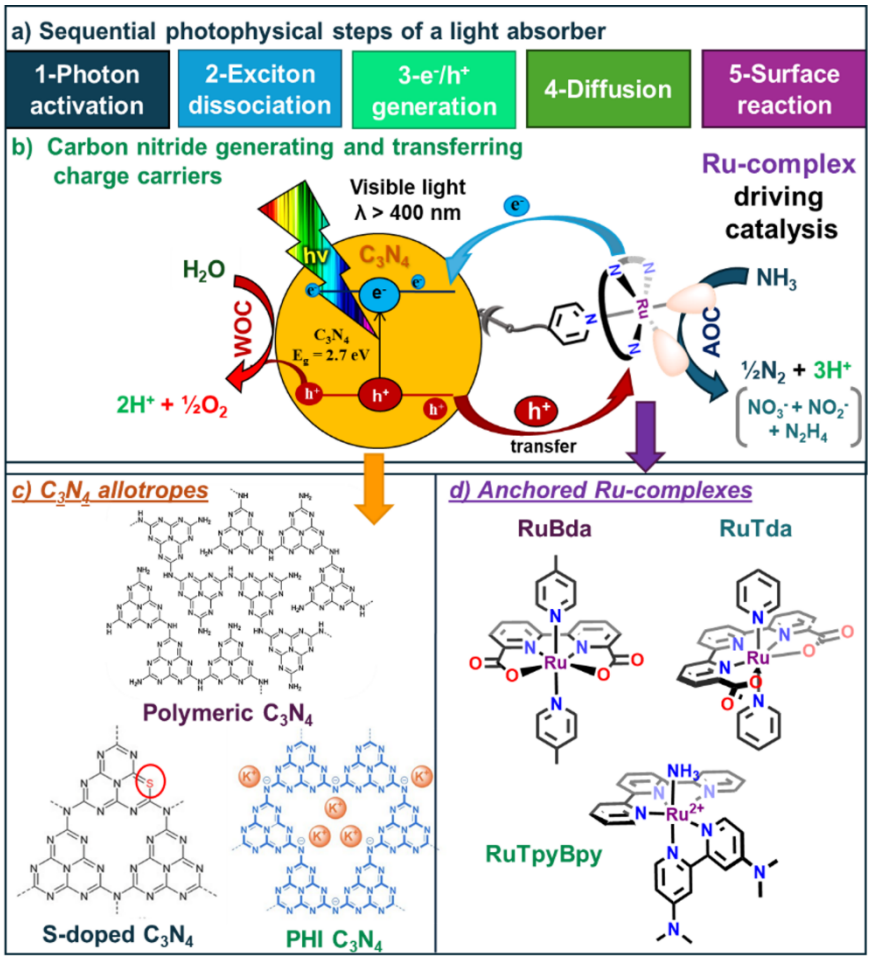


Figure 2: (a) Sequential photophysical and chemical steps of a catalytically active absorber, (b) illustrative scheme of the electron and hole transfer in the RuBda@C_3N_4 interface, (c) three C_3N_4 allotropes, and (d) three Ru-complexes.

surface; and (5) the surface-bound molecular catalyst drives the target redox reaction. Here, either water oxidation or ammonia oxidation at the anchored Ru centre.

This distinction matters especially for C_3N_4. Unlike inorganic semiconductors with high dielectric constants, where exciton formation and dissociation are instantaneous, C_3N_4 has a higher exciton binding energy (0.1–0.4 eV [11]) that makes carrier separation a predominant rate-limiting step. The applied bias in a photoelectrochemical cell assists this dissociation by sweeping free carriers away from the recombination zone, an advantage that goes beyond simply reducing the thermodynamic requirement, and that is discussed further in section G.

C) Carbon nitride as the semiconductor light absorber

C_3N_4 is a transformative organic semiconductor photocatalyst, which has, in fact, over the past decade, transformed into one of the benchmark photocatalysts [12-14]. It is synthesised by solid-state thermal polycondensation of cheap, abundant, nitrogen-rich organic precursors such as melamine, dicyandiamide, or urea at temperatures between 500 and 600 °C, a process requiring no solvents, no metal catalysts, and no complex equipment. The resulting material is a two-dimensional polymer composed of heptazine (tri-s-triazine) or s-triazine building block units linked by tertiary amines into extended graphitic sheets, with a bandgap of approximately 2.7 eV with optical absorption onset at 460 nm (Figure 2b), firmly within the visible range of the solar spectrum [12-14].

C_3N_4 is attractive not only for its multipurpose catalytic platform but also for its light absorption and the simultaneous combination of these properties. Its conduction band edge sits at approximately −1.1 V vs the normal hydrogen electrode (NHE), providing sufficient thermodynamic driving force for many reduction reactions. Its valence band edge at approximately +1.6 V vs NHE supports oxidation chemistry. It is chemically inert to most organic solvents and electrolytes, thermally stable in air up to around 600 °C, and biocompatible. Crucially for hybrid material design, the nitrogen-rich aromatic heptazines contain accessible functional groups, such as primary amines ($–NH_2$) and secondary amines (=NH), thus providing handles for both covalent (e.g. –CO–NH– [15]) and non-covalent (e.g. π–π [16]) attachment of functional molecular guests/appendages [8,12,17].

The C_3N_4 family is not a single material but a rich structural landscape (Figure 2c). Polymeric C_3N_4 (Table 1), the most widely studied form, is semicrystalline, with moderate charge carrier mobility and a bandgap tunable between 2.6 and 2.8 eV, depending on synthesis conditions [12,18]. Poly(heptazine imide) (PHI, Table 1), synthesised in eutectic salt melts, is a highly crystalline ionic variant in which negatively charged nitrogen bridges compensate intercalated metal cations, yielding superior charge carrier mobility, reduced defect density, and extended exciton lifetimes that are of relevance to photoelectrocatalytic performance [19]. Amorphous sulfur-doped C_3N_4 (S-C_3N_4, Table 1), prepared from sulfur-containing precursors such as purpald, achieves a narrower bandgap of 1.8–2.0 eV and a higher surface area, accessing a larger fraction of the solar spectrum at the cost of somewhat reduced charge transport efficiency [13]. Each allotrope presents a distinct combination of optical, electronic, and surface properties, and their comparison in hybrid architectures is itself a source of mechanistic insight.

Beyond allotrope selection, post-synthetic strategies offer a complementary route to tuning the optical and surface properties of polymeric C_3N_4 without resynthesis. Thermal oxidation etching, acid treatment, and alkali-assisted exfoliation can shift the valence band edge, narrow the bandgap, and introduce surface defects that serve as additional anchoring sites or charge-trapping centres, further expanding the parameter space available for hybrid photoelectrode optimization [4,5].

From the perspective of the antenna analogy introduced in section B, C_3N_4 occupies the role of the photosensitizer in the hybrid system. It absorbs visible light, generates electron–hole pairs, and transports these charge carriers to the semiconductor surface where the molecular catalyst awaits [8]. Its medium bandgap means it can harvest blue and green photons that pass

Table 1: Comparison of the key properties of C_3N_4-based materials.

Property	Polymeric C_3N_4	Crystalline PHI	Amorphous S-C_3N_4
structure	semicrystalline	highly ordered	disordered/distorted
bandgap [eV]	2.6–2.8	2.7	1.8–2.0
charge mobility	moderate	high	low
active centres	π–π, NH_x	M^+, N^-, π–π, NH_x	S atom, π–π, NH_x
surface area	moderate: <50 $m^2 \cdot g^{-1}$	low: <30 $m^2 \cdot g^{-1}$	high: <100 $m^2 \cdot g^{-1}$
application focus	versatile, stable	high-performance	high surface reactivity

unused through many metal oxide photocatalysts. Its 2D layered structure, stabilised by π–π stacking interactions between heptazine sheets, provides a large, flat, aromatic surface ideally suited for the non-covalent adsorption of flat aromatic molecular catalysts through complementary π–π and C–H···π interactions [8,16].

D) Ruthenium molecular catalysts: selectivity and multielectron chemistry

Ruthenium is suited for ammonia oxidation for three reasons. First, the six-electron, six-proton oxidation of NH_3 to N_2 requires a metal centre capable of cycling through multiple oxidation states sequentially, Ru(II) through Ru(V), within a narrow and accessible potential window (≈0.2–1.2 V vs NHE), accumulating the oxidizing equivalents needed for N–N bond formation without releasing oxidized intermediates such as hydrazine or hydroxylamine. Second, ammonia is a strong σ-donor that coordinates readily to Ru(II), positioning the substrate in the inner coordination sphere for successive proton-coupled electron-transfer steps. Third, the ligand environment around Ru can be rationally tuned to control the thermodynamics of each Ru(n)/Ru(n + 1) transition, the NH_3/H_2O binding selectivity, and the geometry of the high-valence Ru=NH intermediate that precedes N–N coupling. No first-row transition metal combines oxidation state accessibility, substrate affinity, and ligand tunability with the same reliability, making Ru-based molecular catalysts the benchmark in water oxidation catalysis (WOC) and ammonia oxidation catalysis (AOC).

If C_3N_4 is the antenna and the charge separator, the molecular Ru-complex is the reaction centre, the component that accepts holes from the semiconductor valence band and uses their oxidising power to drive the multielectron, multiproton transformation of the substrate. Ruthenium occupies a privileged position in oxidation catalysis because of its unique ability to access a wide range of stable oxidation states (Ru(II), Ru(III), Ru(IV), Ru(V), and even Ru(VI) under forcing conditions) within a relatively narrow potential window, and because the ligand field around the ruthenium centre can be finely tuned to control the thermodynamics and kinetics of each oxidation step [20,21].

Three benchmark Ru catalysts are particularly relevant to the proposed hybrid strategy (Figure 2d). RuBda (Ru coordinated by 2,2′-bipyridine-6,6′-dicarboxylic acid [22,23]) is the current state-of-the-art catalyst for WOC and AOC [24,25]. Its carboxylate arms provide both strong coordination to the metal and axial or equatorial ligands, which can be conveniently used for surface anchoring, and its low water oxidation onset potential of 1.1 V vs NHE is among the lowest reported for any molecular catalyst [22,24]. When non-covalently attached to carbon paper electrodes through C–H···π interactions, RuBda achieves a turnover number of 7500 and Faradaic efficiency of 100% for electrochemical ammonia oxidation in propylene carbonate, producing N_2 as the sole nitrogen-containing product, a benchmark result that established the molecular framework for AOC [26]. RuTda (Ru coordinated by 2,2′:6′,2″-terpyridine-6,6″-dicarboxylic acid), with its extended terpyridine backbone, has been covalently anchored onto triazine-based covalent organic frameworks (COFs) by Llobet and co-workers, achieving photocatalytic water oxidation with a turnover number of 220 and demonstrating that molecular Ru catalysts retain their activity upon surface immobilisation in photochemical conditions [27]. RuTpyBpy (Ru coordinated by terpyridine and bipyridine), while exhibiting a higher overpotential for water oxidation, has been shown to produce nitrate (NO_3^-) selectively from ammonia oxidation in aqueous media when immobilised on cyclodextrin-functionalized ITO electrodes, illustrating that product selectivity in ammonia oxidation (N_2 vs NO_3^- vs N_2H_4) is tunable through catalyst structure and the reaction environment [28,29].

The mechanistic basis for this selectivity lies in two competing reaction pathways [21,22,30,31]. The unimolecular water/ammonia nucleophilic attack mechanism proceeds when a water or ammonia molecule attacks a high-valence Ru=O or Ru=NH intermediate, generating peroxo or hydrazido species that subsequently release O_2 or N_2 via a series of proton-coupled electron-transfer steps. The bimolecular intermolecular mechanism based on the interaction of two metal units (I2M) proceeds through the coupling of two high-valence Ru species to form a Ru–X–X–Ru (X = O, N) bridged intermediate, releasing O_2 or N_2 upon reductive elimination. Selectivity toward N_2 over hydrazine is thermodynamic: Ammonia oxidation to N_2 is more exergonic than hydrazine formation, which requires a very specific catalyst design to become competitive. Surface immobilisation further disfavours the bimolecular I2M pathway by geometrically constraining adjacent catalyst molecules, but this is a secondary kinetic reinforcement rather than the main selectivity determinant [26,32]. This mechanistic insight is relevant to the design of hybrid C_3N_4–Ru electrodes, where the surface density and spatial arrangement of the anchored catalyst molecules can be controlled through the choice of anchoring chemistry.

E) Covalent and non-covalent anchoring: two routes to the heterointerface

The quality of the C_3N_4–Ru interface, the electronic coupling between the semiconductor and the molecular catalyst, the stability of the catalyst under operating conditions, and the catalyst's accessibility to the substrate depend critically on how the Ru complex is grafted to the C_3N_4 surface. Two different strate-

gies have been developed, each with distinct advantages and limitations [8,17].

Covalent anchoring exploits the amine and imine functional groups that decorate the surface of C_3N_4 because of incomplete polycondensation during synthesis [15]. These $–NH_2$ groups react with activated carboxylic acid derivatives (acyl chlorides or active esters) to form stable amide bonds that link the carbon nitride surface covalently to a bifunctional linker molecule. The linker typically contains a terminal pyridine group at one end, an aromatic or aliphatic bridging moiety, and the reactive acyl group at the other end. Subsequently, a ruthenium precursor then coordinates to the pyridine nitrogen, completing the assembly. The resulting covalent connection is thermodynamically robust, surviving repeated electrochemical cycling and exposure to the reaction medium without significant catalyst leaching. A proof-of-concept, using preliminary unpublished data, to strengthen the credibility of this strategy, RuBda covalently grafted onto polymeric C_3N_4 nanoparticles, achieved a ruthenium surface density of 5.5 mol % Ru (5.5×10^{-4} mol per gram of C_3N_4), validated by ion-coupled plasma and a turnover frequency for ammonia oxidation of 5.6 s^{-1}, surpassing by a few orders of magnitude the activity of the best non-covalently immobilized benchmark. Importantly, transferring the electrode to a fresh electrolyte and performing a rinse test confirmed that catalytic activity follows the electrode rather than dissolved species, confirming that the catalyst remained securely anchored without delamination.

Non-covalent anchoring takes an altogether different approach, exploiting the π-electron density of the aromatic heptazine surface rather than its reactive functional groups [16,32]. Ru complexes functionalized with planar aromatic pyrene groups can adsorb spontaneously onto the C_3N_4 surface through a combination of π–π stacking between the pyrene unit and the heptazine rings, and C–H···π interactions between the aliphatic protons of the complex periphery and the aromatic surface. This one-pot process, that is, dissolving the pyrene-functionalized Ru complex in a suitable solvent, adding the C_3N_4 support, allowing adsorption to reach equilibrium, and washing away excess complex, requires no reactive chemistry and no elevated temperatures, making it synthetically accessible even for complex, sensitive catalyst molecules. The non-covalent strategy has already produced a landmark result: A 15-mer RuTda oligomer non-covalently adsorbed onto C_3N_4 coated on FTO glass achieved a turnover number of 3000 and a turnover frequency of 0.4 s^{-1} for photoelectrocatalytic water oxidation, consuming only micrograms of ruthenium per gram of support, an atom efficiency figure that makes the use of a precious metal economically defensible [16]. Crystalline PHI is a promising support for non-covalent anchoring: Its highly ordered aromatic surface, free of the structural disorder that characterises amorphous C_3N_4, presents a geometrically regular array of π-stacking sites that can accommodate the flat pyrene anchor in a defined orientation, maximising electronic coupling between the catalyst and the semiconductor.

Covalent and non-covalent bonding are not competing alternatives but complementary tools. Covalent anchoring prioritises stability and provides a well-defined, short electron coupling pathway between C_3N_4 and the Ru centre. Non-covalent anchoring prioritises synthetic simplicity and atom efficiency and may be better suited to crystalline PHI, where surface reactivity toward nucleophilic chemistry is lower. Strategies comparison across the three C_3N_4 allotropes, polymeric, PHI, and S-doped amorphous, would reveal structure–activity relationships that cannot be obtained by studying each isolated allotrope.

A third interface strategy, yet to be explored in the C_3N_4–Ru context, is the direct coordination of isolated Ru atoms within the interlayer space of the C_3N_4 scaffold, that is, the single-atom catalyst (SAC) approach. Unlike covalent or non-covalent anchoring of a preformed complex, SACs position individual metal atoms at sub-nanometer proximity to the semiconductor surface, potentially maximizing electronic coupling between antenna and catalytic centre while eliminating the need for a discrete linker or pyrene-functionalized ligand. Open challenges include metal atom migration and agglomeration under prolonged irradiation, and the difficulty of distinguishing genuine single-atom activity from sub-nanometer cluster contributions under operando conditions [33]. A full mechanistic discussion lies beyond the scope of this perspective; SAC nonetheless represents a parallel, and potentially more direct, realization of the antenna–reaction-centre coupling principle that motivates the hybrid strategy described here.

A practical consideration that applies to all anchoring strategies is the photostability of the Ru complex under operating conditions. Ru polypyridyl complexes are among the most photostable molecular catalysts in the WOC and AOC literature [34], and ligand frameworks such as bda and tda are not expected to degrade under visible-light irradiation [15,16,33] The more likely degradation pathways are oxidative cleavage of the amide linker in covalently anchored systems, or displacement of the pyrene anchor by photogenerated reactive oxygen species in non-covalently adsorbed ones, both of which manifest as Ru leaching into solution. The rinse test reported for the RuBda–C_3N_4 covalent system (section E) confirms anchoring integrity under electrochemical conditions, but equivalent stability tests under sustained bandgap illumination remain to be reported and should be considered an essential benchmark,

alongside ICP quantification of Ru leaching and post-catalysis XPS, as demonstrated for analogous Ru(bda)-based electrodes by X-ray absorption spectroscopy after extended bulk electrolysis [26].

F) Why ammonia oxidation?

Ammonia offers compelling thermodynamic advantages as a hydrogen carrier. Its oxidation requires significantly less energy than water splitting, only 33 MJ per kg H_2 at −0.092 V vs NHE, compared to 180 MJ per kg H_2 at 1.23 V vs NHE for the oxygen evolution reaction, representing a substantially lower thermodynamic barrier. Combined with its high volumetric energy density, liquid ammonia stores 1.9 times more energy per liter than liquid hydrogen, making it an attractive medium for carbon-free energy storage and transport [35].

G) The case for photoelectrocatalysis: combining light and bias

Photocatalysis and electrocatalysis each address part of the energy challenge of driving thermodynamically uphill reactions [29,36]. Pure photocatalysis relies entirely on photon energy to supply the thermodynamic driving force, imposing strict requirements on the semiconductor band positions relative to the reaction redox potentials, and offering limited kinetic control. Pure electrocatalysis applies an external potential to drive the reaction, offering precise control of potential but consuming electrical energy that must itself be generated cleanly. Photoelectrocatalysis [19,37], the simultaneous application of light illumination and an electrochemical bias to a semiconductor photoelectrode, combines the advantages of both: Photon energy reduces the required applied potential (the photovoltage generated by the semiconductor partially compensates the thermodynamic requirement of the reaction), while the applied bias provides independent kinetic control over charge carrier dynamics, suppresses recombination by sweeping carriers away from the semiconductor bulk, and enables product selectivity to be tuned by adjusting the electrode potential.

Photoelectrocatalytic ammonia oxidation offers an unexplored and underappreciated advantage. Ammonia oxidation requires the removal of six electrons and six protons (for the N_2 pathway) or eight electrons and nine protons (for the NO_3^- pathway), a multistep process in which each intermediate must be stabilised long enough to undergo the next oxidation event [25,29]. The applied bias in a photoelectrochemical cell keeps the electrode potential within the window required for sequential Ru oxidation (Ru(II)→Ru(III)→Ru(IV)→Ru(V)), while the photogenerated holes from C_3N_4 provide additional oxidising equivalents without requiring the full thermodynamic cost to be met by the external power supply. In this direction, the C_3N_4–Ru hybrid photoelectrode is the synthetic realisation of the Photosystem II concept: Light provides the energy, the semiconductor separates the charges, and the molecular catalyst, precisely positioned at the semiconductor surface through covalent or non-covalent anchoring, does the multielectron bond-breaking chemistry [9].

Despite this compelling conceptual foundation, and despite the availability of all the necessary components, including (a) photoactive C_3N_4 semiconductors in multiple allotropic forms, (b) well-characterised molecular Ru catalysts with demonstrated AOC activity, and (c) established anchoring strategies that preserve catalyst activity upon immobilisation, no study has yet reported the photoelectrocatalytic oxidation of ammonia using a Ru-functionalized C_3N_4 photoelectrode. The closest precedents are the photoelectrocatalytic water oxidation activity of RuTda oligomers on C_3N_4/FTO [16], which confirms the compatibility of the hybrid architecture with the PEC configuration, and the electrocatalytic ammonia oxidation activity of RuBda on carbon paper [26], which confirms that molecular Ru catalysts retain their AOC function upon surface anchoring. The intersection of these two lines of evidence, photoelectrocatalytic AOC at a C_3N_4–Ru hybrid electrode, has not been crossed.

Outlook

The combination of C_3N_4 semiconductors with molecular Ru catalysts through covalent and non-covalent anchoring strategies offers a chemically rational, modern, accessible, and mechanistically transparent route to artificial photosynthetic systems for solar-driven ammonia oxidation, though known and implemented in WOC. Inspired by the design principles of natural photosynthesis, photosensitization, spatial charge separation, and the coupling of a light-harvesting antenna to a multielectron catalytic centre, this hybrid approach addresses the fundamental gap between homogeneous and heterogeneous catalysis by using molecular selectivity and semiconductor light harvesting in the same interfacial architecture. The allotropic diversity of C_3N_4, from semi-crystalline polymeric forms over highly ordered PHI to high-surface-area amorphous S-doped variants, provides a tunable platform for exploring how semiconductor structure controls charge carrier dynamics and thereby catalytic performance.

The step forward is clear in its direction if not yet in its details: It includes fabrication and characterisation of C_3N_4–Ru hybrid photoelectrodes across varying allotropes, Ru catalyst structures, and anchoring chemistries, tested under simultaneous illumination and electrochemical bias in the photoelectrocatalytic ammonia oxidation. That no such study has yet been published is a gap in the literature. The materials components are available, the conceptual framework is established, and the prece-

dent reactions (WOC and electrochemical AOC) have validated the system's key feasibility. Testing them together in photoelectrocatalysis is the experiment that this perspective envisages building toward.

Funding

J.H. thanks the project "The Energy Conversion and Storage", project no. CZ.02.01.01/00/22_008/0004617 by Programme Johannes Amos Comenius, Excellent Research call, for supporting this work. P.J-C. received funding from the European Union's Horizon Europe research and innovation program under the Marie Skłodowska-Curie grant agreement no: 101068996. P.J-C. thanks the Max Planck Society for its financial support.

Author Contributions

Jan Holub: conceptualization; data curation; formal analysis; funding acquisition; investigation; validation; writing – original draft; writing – review & editing. Pablo Jiménez-Calvo: conceptualization; data curation; formal analysis; funding acquisition; investigation; methodology; project administration; validation; writing – original draft; writing – review & editing.

ORCID® iDs

Jan Holub - https://orcid.org/0000-0001-9472-9131
Pablo Jiménez-Calvo - https://orcid.org/0000-0002-9826-6995

Data Availability Statement

Data sharing is not applicable to this article as no new experimental datasets were generated. The discussion draws primarily from previously published studies, which are cited accordingly. Two sets of preliminary unpublished results are included to support the proposed strategy; the underlying data are available from the corresponding authors upon reasonable request and will be reported in full in a forthcoming publication.

References

1. Wang, L.; Shao, M.; Xie, Z.-L.; Mulfort, K. L. *Langmuir* **2024,** *40,* 24195–24215. doi:10.1021/acs.langmuir.4c03249
2. Shen, Y.; Mu, Y.; Wang, D.; Liu, C.; Diaconescu, P. L. *ACS Appl. Mater. Interfaces* **2023,** *15,* 28851–28878. doi:10.1021/acsami.3c01726
3. Reyes Cruz, E. A.; Nishiori, D.; Wadsworth, B. L.; Nguyen, N. P.; Hensleigh, L. K.; Khusnutdinova, D.; Beiler, A. M.; Moore, G. F. *Chem. Rev.* **2022,** *122,* 16051–16109. doi:10.1021/acs.chemrev.2c00200
4. Filippini, G.; Longobardo, F.; Forster, L.; Criado, A.; Di Carmine, G.; Nasi, L.; D'Agostino, C.; Melchionna, M.; Fornasiero, P.; Prato, M. *Sci. Adv.* **2020,** *6,* eabc9923. doi:10.1126/sciadv.abc9923
5. Marchi, M.; Raciti, E.; Gali, S. M.; Piccirilli, F.; Vondracek, H.; Actis, A.; Salvadori, E.; Rosso, C.; Criado, A.; D'Agostino, C.; Forster, L.; Lee, D.; Foucher, A. C.; Rai, R. K.; Beljonne, D.; Stach, E. A.; Chiesa, M.; Lazzaroni, R.; Filippini, G.; Prato, M.; Melchionna, M.; Fornasiero, P. *Adv. Sci.* **2023,** *10,* 2303781. doi:10.1002/advs.202303781
6. Garrido-Barros, P.; Matheu, R.; Gimbert-Suriñach, C.; Llobet, A. *Curr. Opin. Electrochem.* **2019,** *15,* 140–147. doi:10.1016/j.coelec.2019.04.027
7. Wang, J.; Dou, S.; Wang, X. *Sci. Adv.* **2021,** *7,* eabf3989. doi:10.1126/sciadv.abf3989
8. Sharma, C.; Mongal, B. N. *Coord. Chem. Rev.* **2026,** *555,* 217612. doi:10.1016/j.ccr.2026.217612
9. Pantazis, D. A. Natural and Artificial Photosynthesis. In *Solar-to-Chemical Conversion;* Sun, H., Ed.; Wiley: Weinheim, Germany, 2021; pp 41–76. doi:10.1002/9783527825073.ch3
10. Barber, J.; Tran, P. D. *J. R. Soc., Interface* **2013,** *10,* 20120984. doi:10.1098/rsif.2012.0984
11. Melissen, S.; Le Bahers, T.; Steinmann, S. N.; Sautet, P. *J. Phys. Chem. C* **2015,** *119,* 25188–25196. doi:10.1021/acs.jpcc.5b07059
12. Zhen, W.; Xue, C. *Sol. RRL* **2021,** *5,* 2000440. doi:10.1002/solr.202000440
13. Jerigova, M.; Markushyna, Y.; Teixeira, I. F.; Badamdorj, B.; Isaacs, M.; Cruz, D.; Lauermann, I.; Muñoz-Márquez, M. Á.; Tarakina, N. V.; López-Salas, N.; Savateev, O.; Jiménez-Calvo, P. *Adv. Sci.* **2023,** *10,* 2300099. doi:10.1002/advs.202300099
14. Teixeira, I. F.; Jiménez-Calvo, P. Carbon nitrides and titanium dioxide-based photocatalysis outlook and challenges: an overview of hydrogen production, transport, storage, safety, and principles. In *Renewable Energy Production and Distribution;* Jeguirim, M.; Dutournié, P., Eds.; Advances in Renewable Energy Technologies, Vol. 2; Elsevier: London, UK, 2023; pp 145–180. doi:10.1016/b978-0-443-18439-0.00004-5
15. Salati, M.; Mondal, S.; Volokh, M.; Albero, J.; García, H.; Gil-Sepulcre, M.; Shalom, M.; Llobet, A. *Artif. Photosynth.* **2026,** *2,* 43–52. doi:10.1021/aps.5c00019
16. Mondal, S.; Salati, M.; Nicaso, M.; Albero, J.; Segado-Centellas, M.; Volokh, M.; Bo, C.; García, H.; Gil-Sepulcre, M.; Llobet, A.; Shalom, M. *Chem. Sci.* **2024,** *15,* 16546–16553. doi:10.1039/d4sc04678a
17. Majdoub, M.; Anfar, Z.; Amedlous, A. *ACS Nano* **2020,** *14,* 12390–12469. doi:10.1021/acsnano.0c06116
18. Jiménez-Calvo, P.; Marchal, C.; Cottineau, T.; Caps, V.; Keller, V. *J. Mater. Chem. A* **2019,** *7,* 14849–14863. doi:10.1039/c9ta01734h
19. Diab, G. A. A.; Reis, I. F.; Wang, C.; Barreto, D.; Savateev, O.; Teixeira, I. F.; Jiménez-Calvo, P. *Adv. Funct. Mater.* **2025,** *35,* 2501393. doi:10.1002/adfm.202501393
20. Matheu, R.; Ertem, M. Z.; Gimbert-Suriñach, C.; Sala, X.; Llobet, A. *Chem. Rev.* **2019,** *119,* 3453–3471. doi:10.1021/acs.chemrev.8b00537
21. Matheu, R.; Garrido-Barros, P.; Gil-Sepulcre, M.; Ertem, M. Z.; Sala, X.; Gimbert-Suriñach, C.; Llobet, A. *Nat. Rev. Chem.* **2019,** *3,* 331–341. doi:10.1038/s41570-019-0096-0
22. Duan, L.; Bozoglian, F.; Mandal, S.; Stewart, B.; Privalov, T.; Llobet, A.; Sun, L. *Nat. Chem.* **2012,** *4,* 418–423. doi:10.1038/nchem.1301
23. Nakajima, K.; Toda, H.; Sakata, K.; Nishibayashi, Y. *Nat. Chem.* **2019,** *11,* 702–709. doi:10.1038/s41557-019-0293-y
24. Zhang, B.; Sun, L. *J. Am. Chem. Soc.* **2019,** *141,* 5565–5580. doi:10.1021/jacs.8b12862
25. Liu, H.-Y.; Lant, H. M. C.; Cody, C. C.; Jelušić, J.; Crabtree, R. H.; Brudvig, G. W. *ACS Catal.* **2023,** *13,* 4675–4682. doi:10.1021/acscatal.3c00032
26. Beiler, A. M.; Denisiuk, A.; Holub, J.; Sánchez-Baygual, F.-J.; Gil-Sepulcre, M.; Ertem, M. Z.; Moonshiram, D.; Piccioni, A.; Llobet, A. *ACS Energy Lett.* **2023,** *8,* 172–178. doi:10.1021/acsenergylett.2c02483

27. Salati, M.; Dorchies, F.; Wang, J.-W.; Ventosa, M.; González-Carrero, S.; Bozal-Ginesta, C.; Holub, J.; Rüdiger, O.; DeBeer, S.; Gimbert-Suriñach, C.; Durrant, J. R.; Ertem, M. Z.; Gil-Sepulcre, M.; Llobet, A. *Small* **2025,** *21,* 2406375. doi:10.1002/smll.202406375
28. Sévery, L.; Szczerbiński, J.; Taskin, M.; Tuncay, I.; Brandalise Nunes, F.; Cignarella, C.; Tocci, G.; Blacque, O.; Osterwalder, J.; Zenobi, R.; Iannuzzi, M.; Tilley, S. D. *Nat. Chem.* **2021,** *13,* 523–529. doi:10.1038/s41557-021-00652-y
29. Kostopoulos, N.; Robert, M.; Sekretareva, A. *ChemElectroChem* **2024,** *11,* e202300462. doi:10.1002/celc.202300462
30. Dunn, P. L.; Cook, B. J.; Johnson, S. I.; Appel, A. M.; Bullock, R. M. *J. Am. Chem. Soc.* **2020,** *142,* 17845–17858. doi:10.1021/jacs.0c08269
31. Ding, X.; Ji, Y.; Huang, H.; Huang, J.; Chen, S.; Yang, C.; Li, F.; Luo, M. *Chem Catal.* **2024,** *4,* 100932. doi:10.1016/j.checat.2024.100932
32. Gil-Sepulcre, M.; Lindner, J. O.; Schindler, D.; Velasco, L.; Moonshiram, D.; Rüdiger, O.; DeBeer, S.; Stepanenko, V.; Solano, E.; Würthner, F.; Llobet, A. *J. Am. Chem. Soc.* **2021,** *143,* 11651–11661. doi:10.1021/jacs.1c04738
33. Melchionna, M.; Fornasiero, P. *J. Am. Chem. Soc.* **2025,** *147,* 2275–2290. doi:10.1021/jacs.4c15803
34. Hennessey, S.; González-Gómez, R.; McCarthy, K.; Burke, C. S.; Le Houérou, C.; Sarangi, N. K.; McArdle, P.; Keyes, T. E.; Cucinotta, F.; Farràs, P. *ACS Omega* **2024,** *9,* 13872–13882. doi:10.1021/acsomega.3c08800
35. Adli, N. M.; Zhang, H.; Mukherjee, S.; Wu, G. *J. Electrochem. Soc.* **2018,** *165,* J3130–J3147. doi:10.1149/2.0191815jes
36. Yang, J.; Wang, D.; Han, H.; Li, C. *Acc. Chem. Res.* **2013,** *46,* 1900–1909. doi:10.1021/ar300227e
37. Bora, L. V.; Bora, N. V. *Fuel* **2025,** *381,* 133642. doi:10.1016/j.fuel.2024.133642

License and Terms

This is an open access article licensed under the terms of the Beilstein-Institut Open Access License Agreement (https://www.beilstein-journals.org/bjnano/terms), which is identical to the Creative Commons Attribution 4.0 International License (https://creativecommons.org/licenses/by/4.0). The reuse of material under this license requires that the author(s), source and license are credited. Third-party material in this article could be subject to other licenses (typically indicated in the credit line), and in this case, users are required to obtain permission from the license holder to reuse the material.

The definitive version of this article is the electronic one which can be found at:
https://doi.org/10.3762/bjnano.17.61

BEILSTEIN JOURNAL OF NANOTECHNOLOGY

Nonprecious bifunctional electrocatalysts for oxygen electrode reactions

Shaheen Parveez Bhuyan, Bhrigu Kumar Pegu, Darshan Jyoti Gogoi, Pragya Moni Gogoi and Pankaj Bharali*§

Review

Open Access

Address:
Department of Chemical Sciences, Tezpur University, Napaam 784028, Assam, India

Email:
Pankaj Bharali* - pankajb@tezu.ernet.in

* Corresponding author
§ Tel. +91 3712 275064

Keywords:
bifunctionality; electrocatalysis; non-precious electrocatalyst; oxygen evolution reaction; oxygen reduction reaction

Beilstein J. Nanotechnol. **2026,** *17,* 1302–1319.
https://doi.org/10.3762/bjnano.17.90

Received: 13 April 2026
Accepted: 18 August 2026
Published: 24 September 2026

This article is part of the thematic issue "Sustainable nanomaterials for energy conversion and environmental remediation".

Guest Editor: P. Jiménez-Calvo



© 2026 Bhuyan et al.; licensee Beilstein-Institut.
License and terms: see end of document.

Abstract

The two most crucial reactions in energy storage and conversion systems are oxygen reduction reaction (ORR) and oxygen evolution reaction (OER). However, their sluggish kinetics arise the need for commercially feasible bifunctional electrocatalysts to assist the reaction by improving its kinetics at the same time ensuring durability and also taking cost into account. The fundamentals of the oxygen electrodes are discussed followed by various techniques adopted by researchers to tune the electronic structures of carbon- and transition metal-based nanostructures towards enhanced activity in ORR/OER. Emphasis is placed on correlating catalyst structure/composition with electrocatalytic properties, simultaneously highlighting the persistent challenges. Hence, the review provides an overview on the recent advances in the field of non-precious bifunctional electrocatalysts for oxygen electrode reactions, which will serve as a foundation for their application in various fields including metal–air batteries.

Introduction

Traditional energy resources are becoming scarcer as societies and economies grow because of widespread consumption of fossil fuels. This overreliance on fossil fuels has caused severe environmental degradation resulted in glacier melting, depletion of the ozone layer, rising sea levels, and an increase in global temperatures. Hence addressing these challenges has become a critical priority in the modern era. To reduce energy constraints and environmental deterioration, the development of sustainable and environmentally benign energy conversion and storage technologies is essential. Regarding innovative technologies that lessen the carbon footprint, electrocatalysis has taken the forefront. Electrochemistry is crucial because it allows interconversion between electrical and chemical energy, providing surplus electrical energy, particularly from renewable sources to be stored in the form of chemical energy or utilized to drive non-spontaneous reactions. Conversely, energy shortages can

occasionally be compensated by transforming stored chemical energy into electrical energy through natural electrochemical processes that take place in galvanic cells helping to balance energy supply and demand [1-3].

Recently, the improvement of effective and inexpensive energy tools has drawn a lot of research interest around efficient, low-cost, and green energy technologies. Water electrolyzers, fuel cells, organic solar cells, and metal–air batteries are regarded as promising, clean, and efficient for sources in the traditional energy sector due to their minimal environmental impact and higher energy transition efficacy. Using advanced sustainable electrochemical conversion technologies and catalytic principles reduces the dependence on fossil fuel-based energy sources [4].

Review

Fundamentals of oxygen electrode reactions

The electrocatalytic conversion of oxygen comprises oxygen reduction reaction (ORR) and oxygen evolution reaction (OER). ORR takes place at the cathode, whereas OER occurs at the anode. Both reactions proceed through multistep electron-transfer pathways, which ultimately govern the reaction kinetics. Notably, ORR and OER are four-electron reaction processes that result in intrinsically slow kinetics and higher overpotentials [5,6]. Pt/C is the standard catalyst for ORR, while Ir/Ru oxides have demonstrated exceptional stability and durability for OER. However, the high cost and limited availability of these precious noble-metal based catalysts restrict their large-scale practical applications. Pt-based catalysts have a strong ORR activity but poor OER performance due to the formation of surface Pt oxides that develop at high overpotentials and possess low electrical conductivity. In contrast, for OER, RuO_2 and IrO_2 show superior catalysis but are poor in ORR performance [1,7]. Therefore, it is essential to concentrate on creating a suitable bifunctional OER/ORR catalyst that replaces noble metal catalysts with inexpensive, abundant, and highly active non-noble metal catalysts. The most common approach of identifying a good bifunctional catalyst for ORR and OER is to measure its overpotential based on the same catalyst loading and at a specific current density. A promising bifunctional catalyst is indicated by a smaller overpotential at a specific rate. Additionally, a bifunctional catalyst that is both highly active and stable enough to cope with the challenging conditions faced during ORR and OER needs to be developed [6].

In recent years, transition metal (TM)-based and carbon-based materials appeared as promising candidates for bifunctional ORR/OER electrocatalysts. Their favourable catalytic properties, including higher activity, high surface area, selectivity, and tunable electronic structures, make them suitable for enhancing the electrochemical performance in energy storage and conversion applications. Transition metals, such as, Fe, Co, Mn, Ni, Cu, and Mo, and their compounds are highly desirable due to their cost-effectiveness, catalytic activity and compositional diversity. In comparison to noble metals like Pt, and Ir, TMs are more abundant and less expensive [8]. TM compounds can be classified into several categories based on their composition and structure, including metal–organic frameworks (MOFs) [9], alloys [10], hydroxides [11], dichalcogenides, phosphides, and nitrides [12,13]. Among these, transition metal alloys benefit from synergetic effects that can enhance performance via modifications in electronic structure and active sites. Furthermore, the catalytic activity of TM-based catalysts is quite comparable to that of noble metal-based catalysts. The performance of transition metal-based catalysts can be enhanced through doping or forming heterostructures. Surface chemical activity and charge transport characteristics can be modulated by doping metals and non-metals [14,15].

Strategies aimed at optimizing the intrinsic catalytic activity of non-precious metal electrocatalysts are fundamentally guided by the Sabatier principle. It states that the interaction between a catalyst surface and reaction intermediates must be perfectly balanced, that is, neither too strong nor too weak. A number of electronic structural factors such as d-band centre, e_g orbital occupancy, adsorption energies, density of states, and spin ordering have been identified as key descriptors in order to assess the bonding strength between reactants and active sites. These descriptors have emerged as valuable tools for understanding and predicting catalytic behaviour through quantitative structure–activity relationships. Among the descriptors, e_g occupancy and d-band centre are the most prevalent for predicting the activities of ORR catalysts; for OER catalysts, e_g occupancy and metal–oxygen covalency are most widely used [16]. In TM-based catalysts, the position of the d-band centre relative to the Fermi level influences the adsorption strength of oxygen-containing intermediates (*OH, *O, and *OOH), thereby affecting ORR and OER kinetics. Similarly, transition-metal cations have an e_g orbital filling close to unity, which often correlates with optimal oxygen intermediate adsorption and enhanced OER activity [17]. In addition, adsorption energies of key reaction intermediates serve as quantitative indicators of catalytic efficiency and can be used to establish volcano-type relationships between catalyst composition and activity [18]. Accordingly, a number of electronic structure engineering techniques have been set forward to maximize the intrinsic activity of a single catalytic site through generation of vacancies, heteroatom doping, and interface design [19].

Likewise, carbon-based materials have drawn great attention as electrocatalysts due to their cost-effectiveness, high surface

area, superior electrical conductivity, economic viability, and strong synergistic interactions with other catalytic components. Carbon-based catalysts include carbon nanotubes (CNTs), graphene, and carbon black [18,20]. Graphene, a 2D single layer of sp^2-bonded carbon atoms, and CNTs, known for their exceptional conductivity and surface area, have shown promising bifunctional activity towards both ORR and OER, even as metal-free catalysts in certain cases [21,22]. A typical approach for determining the superior bifunctional catalytic performance for ORR and OER is to measure the overpotential required to achieve a specific current density using the same catalyst loading for both ORR and OER. A lower overpotential at a given current density indicates superior bifunctional activity. Nanomaterials have distinctive properties that significantly enhance OER and ORR kinetics [15].

To date, several excellent review publications have summarized the progress of oxygen electrocatalysts, with emphasis on specific catalyst classes, important descriptors for catalytic activity, as well as synthetic strategies and practical applications [14,18,20-22]. In contrast, this review begins with a discussion of fundamental reaction mechanisms of ORR/OER, followed by discussion of various types of nanostructured catalysts like transition metal-based catalyst, carbon-based materials, their roles in improving ORR/OER performance, and developments in the design and synthesis of heterogeneous bifunctional electrocatalysts. Particular emphasis is placed on correlating catalyst composition and electronic structure with electrocatalytic performance through key activity descriptors of oxygen intermediates. Finally, the study explores current challenges and future directions in oxygen electrocatalysis.

Reaction mechanisms of ORR and OER

The ORR operates at the cathode of fuel cells and metal–air batteries during discharge. The OER takes place while charging metal–air batteries or during water splitting [23,24]. The primary element of the oxygen electrode is the catalyst activation layer, where adsorbed oxygen participates in electrochemical processes that occur at the gas–liquid–solid three-phase boundary [25]. It involves multistep, slow proton-coupled electron-transfer processes in both ORR and OER, resulting in high overpotentials and low energy efficiency, underscoring the need for effective bifunctional electrocatalysts.

ORR mechanism. ORR represents one of the most vital processes studied in modern electrochemistry. It is either a two-electron process, which is linked to terminal oxygen adsorption and generates intermediate H_2O_2, or the complete transformation of molecular oxygen into water through a direct four-electron transfer process by bidentate oxygen adsorption [26-30]. The combination of rapid kinetics, effective electron transfer, and strong energy efficiency contributes to its appeal, with no reactant molecule loss and environmentally friendly reaction products. Four-electron reduction is ideal in the progress of distinct green energy strategies, for example, electrochemical energy conversion as well as storage [9]. In addition to producing corrosive products (H_2O_2), the indirect four-electron reaction and OH^- ions damage the catalyst and diminish the potential of the oxygen reduction electrode, hence decreasing battery efficiency. Therefore, the indirect four-electron reaction should be avoided as much as feasible [25].

In the direct four-electron process, the adsorption and activation of O_2 molecules on the catalyst's surface is a crucial stage. It proceeds through a series of surface or interfacial processes. Further, the reactions proceed via electron transfer, chemical bond breaking, molecular restructuring, and the creation of reaction products, which are ultimately discharged from the catalyst surface. Its activation is facilitated by stable O_2 adsorption behaviour [31,32]. The processes of M–OH, M–O, and M–OOH adsorption and desorption are recognised as very significant in the reaction process, regardless of acidic or alkaline environments [33,34]. A detailed mechanistic route in both acidic and alkaline media is shown in Figure 1a,b and Table 1.

OER mechanism. Often regarded as the main obstacle in bifunctional oxygen electrodes, the OER has sluggish kinetics that constrains the capability to convert energy efficiently. Many studies over the past few years have focused on the development and understanding of OER. Numerous studies have been conducted utilizing density functional theory (DFT) simulations to examine the OER. Under both acidic and alkaline conditions, the commonly established OER process consists of four-electron/proton transfer steps [37]. During the OER mechanism, M–OH, M–O, and M–OOH species are adsorbed onto the crucial active site (M) of the electrocatalyst, which leads to the formation of O_2 [38,39]. Under acidic conditions, H_2O is dissociated to OH^- and gets adsorbed at the active site [6]. Under basic conditions, hydroxide ions first produce hydroxy intermediates (M–OH) by adhering to the electrocatalyst surface. After reacting with other OH^- ions, these intermediates create hydroperoxide species (M–OOH), which are then followed by the creation of O–O bonds [40]. A detailed mechanistic route in both acidic and alkaline media for OER is shown in Figure 1c,d.

The ORR and OER processes proceed via the continuous formation and transformation of intermediates at the catalytically active site. The catalytic activity and reaction energetics are largely determined by the adsorption behaviour of these intermediates. As a result, M–OH, M–O, and M–OOH adsorption free energies are commonly acknowledged as important indica-

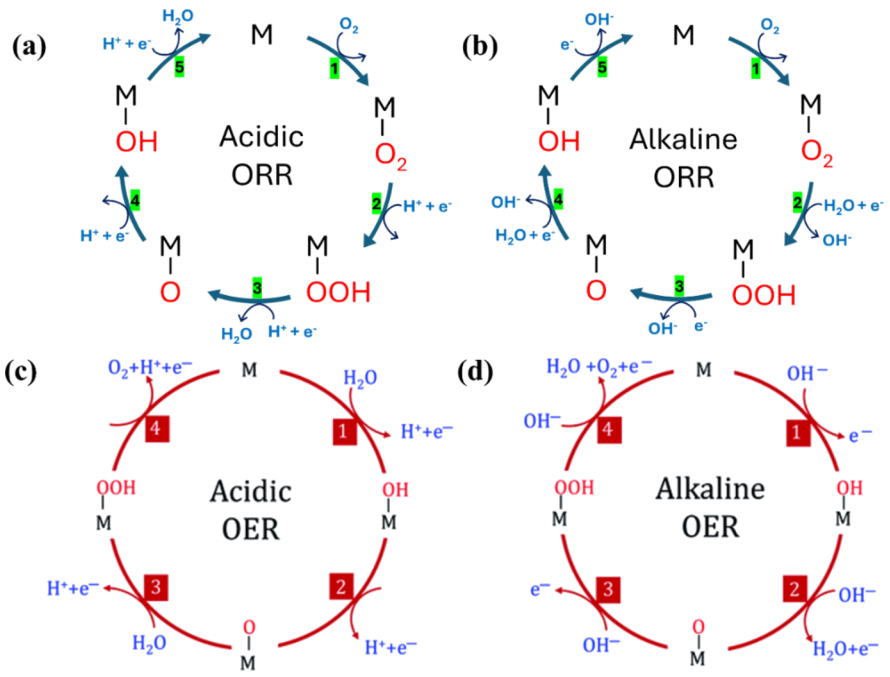


Figure 1: Schematic reaction mechanisms under (a) acidic and (b) alkaline conditions for ORR [35], and under (c) acidic and (d) alkaline conditions for OER [36] (Figure 1c and d was adapted from [36] © 2020 Z. Yan et al., published by Royal Society of Chemistry, distributed under the terms of the Creative Commons Attribution 3.0 Unported License, https://creativecommons.org/licenses/by/3.0/.)

Table 1: Mechanistic pathways and thermodynamic parameters of ORR and OER under acidic and alkaline conditions [32,33].

Reaction pathway	Medium	Specific mechanistic route	Surface intermediates	Thermodynamic parameters (overall reaction)
ORR ($4e^-$ route)	acidic	$M + O_2 \rightarrow M–O_2$ $M–O_2 + H^+ + e^- \rightarrow M–OOH$ $M–OOH + H^+ + e^- \rightarrow M–O + H_2O$ $M–O + H^+ + e^- \rightarrow M–OH$ $M–OH + H^+ + e^- \rightarrow M + H_2O$ overall reaction: $O_2\ (g) + 4H^+(aq) + 4e^- \rightarrow 2H_2O(liq)$	$M–O_2 \rightarrow M–OOH \rightarrow M–O \rightarrow M–OH$	$E° = 1.229$ V vs RHE $\Delta G° = -4.92$ eV
ORR ($4e^-$ route)	basic	$M + O_2 \rightarrow M–O_2$ $M–O_2 + H_2O + e^- \rightarrow M–OOH + OH^-$ $M–OOH + e^- \rightarrow M–O + OH^-$ $M–O + H_2O + e^- \rightarrow M–OH + OH^-$ $M–OH + e^- \rightarrow M + OH^-$ overall reaction: $O_2\ (g) + 2H_2O\ (liq) + 4e^- \rightarrow 4OH^-\ (aq)$	$M–O_2 \rightarrow M–OOH \rightarrow M–O \rightarrow M–OH$	$E° = 1.229$ V vs RHE $\Delta G° = -4.92$ eV
ORR ($2e^-$ route)	acidic	$M + O_2 \rightarrow M–O_2$ $M–O_2 + H^+ + e^- \rightarrow M–OOH$ $M–OOH + H^+ + e^- \rightarrow M + H_2O_2$ overall reaction: $H_2O_2\ (liq) + 2H^+\ (aq) + 2e^- \rightarrow 2H_2O\ (liq)$	$M–O_2 \rightarrow M–OOH$	H_2O_2 formation (no $\Delta G°$ reported)
ORR ($2e^-$ route)	basic	$M + O_2 \rightarrow M–O_2$ $M–O_2 + H_2O + e^- \rightarrow M–OOH + OH^-$ $M–OOH + e^- \rightarrow M + OH_2^-$ overall reaction: $O_2\ (g) + H_2O\ (liq) + 2e^- \rightarrow HO_2^-\ (aq) + OH^-\ (aq)$	$M–O_2 \rightarrow M–OOH$	OH_2^- formation (no $\Delta G°$ reported)

Table 1: Mechanistic pathways and thermodynamic parameters of ORR and OER under acidic and alkaline conditions [32,33]. (continued)

OER	acidic	H_2O (liq) + M → M–OH + H^+ + e^- M–OH → M–O + H^+ + e^- H_2O (liq) + M–O → M–OOH + H^+ + e^- M–OOH → M + O_2 (g) + H^+ + e^- overall reaction: $2H_2O$ (liq) → O_2 + $4H^+$ + $4e^-$	M–OH→ M–O → M–OH	$E°$ = 1.229 V vs RHE $\Delta G°$ = +4.92 eV
OER	basic	M + OH^- → M–OH + e^- M–OH + OH^- → M–O + H_2O (liq) + e^- M–O + OH^- → M–OOH + e^- M–OOH + OH^- → M + O_2 (g) + H_2O (liq) + e^- overall reaction: $4OH^-$ → O_2 (g) + $2H_2O$ (liq) + $4e^-$	M–OH → M–O → M–OH	$E°$ = 1.229 V vs RHE $\Delta G°$ = +4.92 eV

tors for assessing the intrinsic activity of ORR and OER electrocatalysts. In order to facilitate formation, conversion, and desorption of these intermediates during the reaction, an effective catalyst should have modest adsorption strengths. This concept is often demonstrated using activity volcano plots, where catalysts positioned around the volcano apex display adsorption energetics close to the optimum, thus providing enhanced electrocatalytic performance with reduced overpotentials [31,38,39]. Affordable and highly efficient bifunctional electrocatalysts having stable O_2 and OH^- adsorption behaviour are currently needed. This review will elaborate on how carbon-based and non-precious transition metal-based electrocatalysts have been the popular candidates for such bifunctional oxygen electrodes.

Bifunctional oxygen electrocatalysts

In recent decades, a variety of extremely efficient electrocatalysts made from non-precious materials have been designed and utilized for bifunctional ORR/OER reactions. Materials based on non-precious transition metals and carbons have demonstrated significant promise in electrochemical applications [41]. The increased surface area and exceptional electrically conductive nature of carbon-based materials help to increase ORR/OER activity. However, many carbon-based electrocatalysts face durability issues in the intense oxidative environment at high OER potentials, while transition metal-based electrocatalysts remain stable under such conditions [42]. Attaining a well-balanced performance that encompasses both ORR and OER capabilities is crucial for evaluating the catalytic effectiveness of a catalyst with bifunctionality towards its application in energy storage and energy conversion systems as displayed in Figure 2 [43].

The bifunctionality index (BI), that is, the potential difference ($\Delta E = E_{j=10} - E_{1/2}$), where $E_{j=10}$ is for OER and the $E_{1/2}$ for ORR, is a crucial performance metric ($E_{j=10}$ indicates the potential at current density 10 mA·cm^{-2}, and $E_{1/2}$ indicates the half-wave potential). A lower potential for $E_{j=10}$ or a more positive $E_{1/2}$ means the catalyst possesses either a higher exchange current density; this means that the electrode surface has more active sites, better intrinsic conductivity, or faster charge-transfer kinetics, which allow the oxidation or the reduction to occur faster. Therefore, a smaller ΔE value signifies superior oxygen electrode activity and greater reversibility, highlighting the catalyst's effectiveness [44]. The BI is derived from the simple calculation of $j(\eta_{OER})$ and $j(\eta_{ORR})$ from the current density (j) vs electrode potential (E) curve using voltammetry data [45]. While voltammetry tests provide a fast and straightforward experimental approach to determine the BI, it is important to recognize that discovering materials with outstanding bifunctional performance remains quite challenging. This difficulty largely stems from differences in the active sites involved in the OER and ORR, which are often altered by changes to the catalyst surface caused by the applied electrode potentials [46].

Carbon-based materials

Currently, carbon-based materials are most widely used in the preparation of electrode materials because of their high availability, high conductivity, strong tolerance towards acid/alkaline condition, and low cost. Here, various aspects of the use of carbon-based materials as bifunctional electrocatalysts for ORR and OER are discussed.

Defective carbon/defect engineering. Carbon materials, like any other material, are not defect-free crystals. The defects are critical to the intrinsic properties of the carbon materials towards electrocatalysis. Hence, regulating such defects can ensure optimized OER and ORR catalytic activity, which is called defect engineering [47-49]. Intrinsic carbon defects include edges, vacancies, and topological defects [50]. These defects can affect the electrocatalytic activity by modifying the surface properties and electronic structure of the substrate [51]. Therefore, introducing intrinsic defects by defect engineering either modulates the p-orbital alignment, narrows the bandgap,

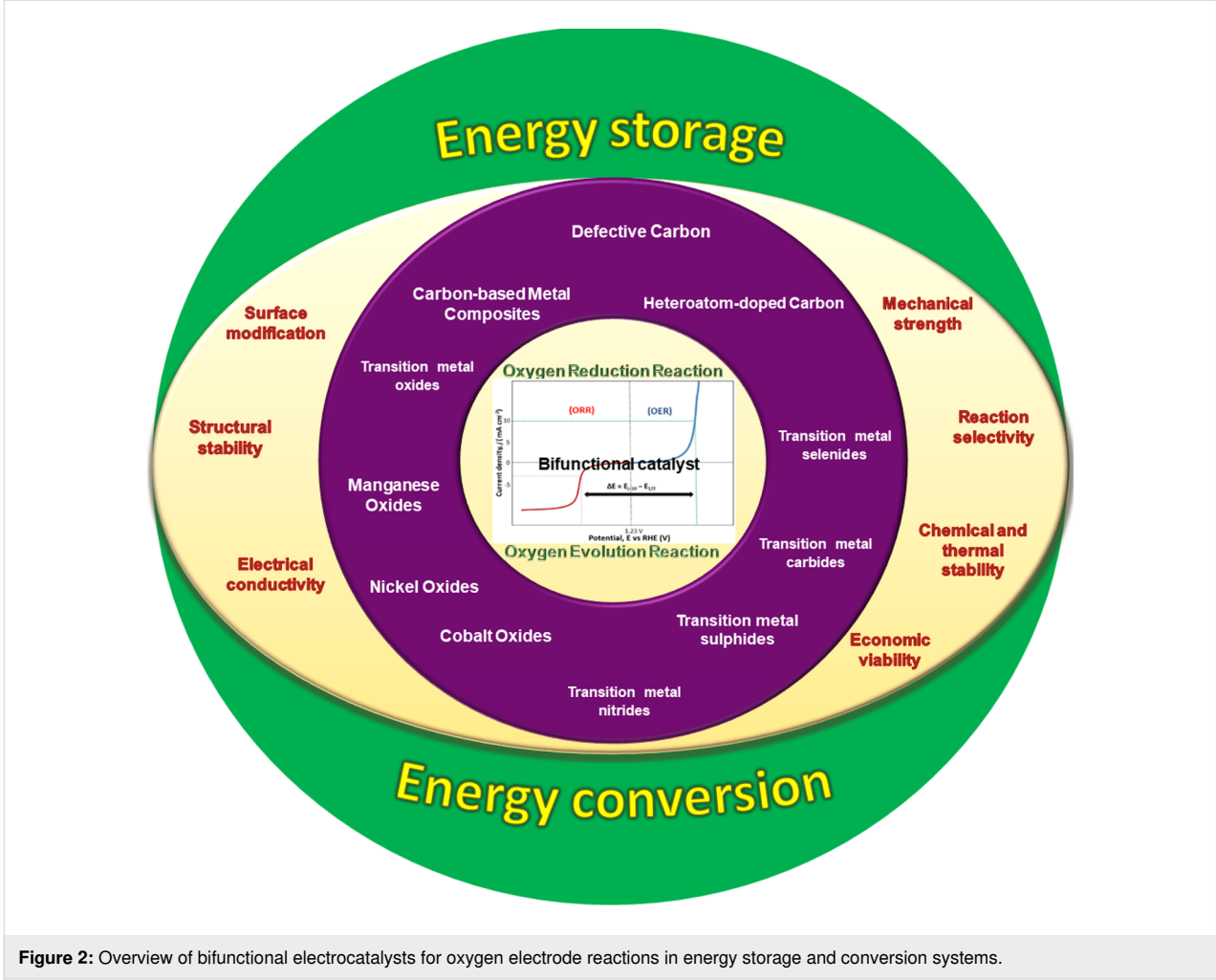


Figure 2: Overview of bifunctional electrocatalysts for oxygen electrode reactions in energy storage and conversion systems.

or breaks the uniform π conjugation of the carbon framework accelerating the kinetics as well as creating active sites for the interaction of oxygen intermediates. This section will be discussing how intrinsic defect engineering can correlate to the understanding of electrocatalytic activity of a catalyst towards an electrochemical reaction.

Edges are the most common defects among the intrinsic carbon defects. Different electrochemical and thermodynamic properties are related to the edges depending on the states in which the edge and basal planes interact with each other [52]. A carbon atom at the edge with sp^2 hybridization has a catalytic activity by a factor of two higher than a carbon atom in the bulk [53]. Tao et al. found that carboxylic groups at the defected edges, together with localised unpaired electrons facilitate intermolecular arrangements. These features work in tandem to effectively capture molecular oxygen, thereby improving the kinetics of the catalysis [54]. In a hexagonal carbon skeleton, there are two types of edges, armchair and zigzag edges [54]. Research revealed that due to the abundance of unpaired π electrons at the zigzag edge sites, the energy required to promote the formation of OOH^* from oxygen molecules is lower. However, a DFT calculation reported by Xia and co-workers also suggested that defects at the armchair edges of graphene showed lower overpotential than zigzag edge defects [55]. Holes or vacancies are another type of intrinsic defects in the basal plane of carbon. Vacancy defects occur when one to few carbon atoms are missing from the lattice, while hole defects involve missing of a large number of atoms. However, vacancy or hole defects are usually accompanied by edge defects. Dai and his group reported the synthesis of a graphitic surface with abundance of stereoscopic holes, which ensured high surface area and high pore volume, with abundant interfacial active surface area and good electron/electrolyte transfer enhancing the overall electrocatalytic activity of the catalyst towards ORR and OER [56].

Topological defects in carbon, also known as lattice imperfection, cause non-hexagonal structures like Stone–Wales (SW) defects in the carbon framework [57,58]. SW defects are prevalent topological defects in planar low-dimensional structures.

Khan et al. developed a synthetic strategy of absorption–calcination, to fabricate SW defects to allow the incorporation of Ni and Fe into structure. It was found that the defect-rich carbon support enhanced the bifunctional activity of the catalyst and also provided control over agglomeration of Ni and Fe atoms [59].

Heteroatom-doped carbon. Hetero-doping the carbon skeleton with elements such as N, P, S, O, B, or F introduces a redistribution of electrons due to the difference in atomic size, bond length and also, electronegativity between the dopant and the carbon; this enables the catalyst to provide more active sites. Conceptually, doping nitrogen into a carbon-based material will cause the carbon to acquire positive charge by delocalisation, which will make such centres active sites for ORR [60]. Xia and co-workers established a volcano plot for the lower limit of overpotential of various p-block elements doped in graphene versus the descriptor Φ to correlate the binding energy with the ORR/OER activity of a metal-free heteroatom-doped carbon catalyst, where Φ is the dimensionless product of relative electron negativity (of the doping element relative to carbon) and electron affinity. According to the volcano plot, nitrogen was the most active dopant towards the ORR, whereas for OER, phosphorus exhibited the lowest overpotential [60]. Also, N-doped carbon is the most extensively studied heteroatom-doped carbon-based electrocatalyst because of the similar size of nitrogen atoms and carbon atoms with much higher electronegativity; less studies have been carried out for phosphorus due to its size and the difficulties in introducing it into the carbon matrix [61]. For example, Li and co-workers synthesized a wrinkled carbon nanosphere doped with nitrogen by a soft-template method. This improved the catalytic performance of both ORR and OER by providing a protective shell against agglomeration of M–Nx active sites and preventing alloy corrosion by accelerated surface layer reconstruction. The wrinkles on the nanospheres immobilized the active sites, thereby preventing them from agglomeration [62].

Recently, Yang et al. established a CoFe@($Co_{0.5}Fe_{0.5}$)S N-doped carbon nanotube heterostructured catalyst, which achieved an exceptionally high peak power density of 136.0 $mW{\cdot}cm^{-2}$, much higher than that of the commercially available Pt/C+ RuO_2 (102.2 $mW{\cdot}cm^{-2}$). It conveyed a cycling efficiency of 48.5% after the 800th cycle and operated stably for more than 10,000 min. The strong interfacial coupling within the heterostructure and sulfur-induced electronic modulation, which reduced *OH and *OOH absorption, resulted in the enhanced catalytic performance in both ORR and OER. The catalyst was used in a rechargeable zinc–air battery (ZAB) as a bifunctional oxygen electrocatalyst with very high performance and durability [63]. Another study of heteroatom-doped C, which had N and S doped into graphene oxide, showed superior catalytic properties towards both OER and ORR. The N,S-doped graphene (NSG) was distributed uniformly throughout the surface, which resulted in increased exposure of active sites as shown by the TEM and SEM images in Figure 3a–d. The ORR performance of NSG was compared with that of commercial Pt/C (20%) (Figure 3e), which exhibited onset potential at 0.95 V vs RHE, comparable to the commercial catalyst. Also, a current density of 10 $mA{\cdot}cm^{-2}$ was achieved at 1.62 V, as shown in the OER linear sweep voltammograms of Figure 3f. This can be attributed to the increased spin density and the facilitated charge transfer due to the mismatch of the outermost orbitals of C and S [64].

The explanation for this is the substitution of larger S atoms into the sp^2 framework of carbon, which introduces substantial localized structural strain, breaking the symmetry of the conjugated network. The mismatch between the relatively localized C 2p orbitals and the more diffuse S 3p orbitals lowers the charge-transfer resistance and creates fast electron-conduction pathways. The co-doping of N and S into the graphitic network breaks the electroneutrality, optimizing the adsorption free energies of electrochemical intermediates and facilitating rapid faradaic charge transfer across the catalyst–electrolyte interface [60,61]. Wang et al. designed a facile silica xerogel strategy using economic biomass material to synthesise the N-doped carbon network (Co-N-C SAC) shown in Figure 3g. The synthesis process began with the Stöber method to form silica-supported structures, which then underwent freeze-drying. Subsequent pyrolysis under an inert atmosphere enabled the incorporation of nitrogen-doped carbon and cobalt into the silica framework. Finally, acid etching was performed to refine the composite structure. This strategy generated massive mesopore and micropores, which resulted in an outstanding performance of Co–N–C SAC as bifunctional electrocatalyst in alkaline medium in a ZAB [65].

Carbon-based metal composites. OER/ORR typically include both electrolyte and oxygen mass transfer and electrical conduction among the active sites and the remaining surface of the electrode. Hence, continuous and efficient transfer between the active sites and the surface ensures better performance of the catalyst. The previous section demonstrated that the creation of defects and heteroatom doping could enhance the performance of the catalyst towards ORR/OER; however, the durability of carbon at high potentials is quite a challenge when it comes to OER. Composites of carbon materials with transition metal compounds are one of the approaches to attain better catalyst activity. Individual components that show good catalytic activity towards ORR or OER can be combined in composites and exhibit strong interfacial chemical interaction and electrical

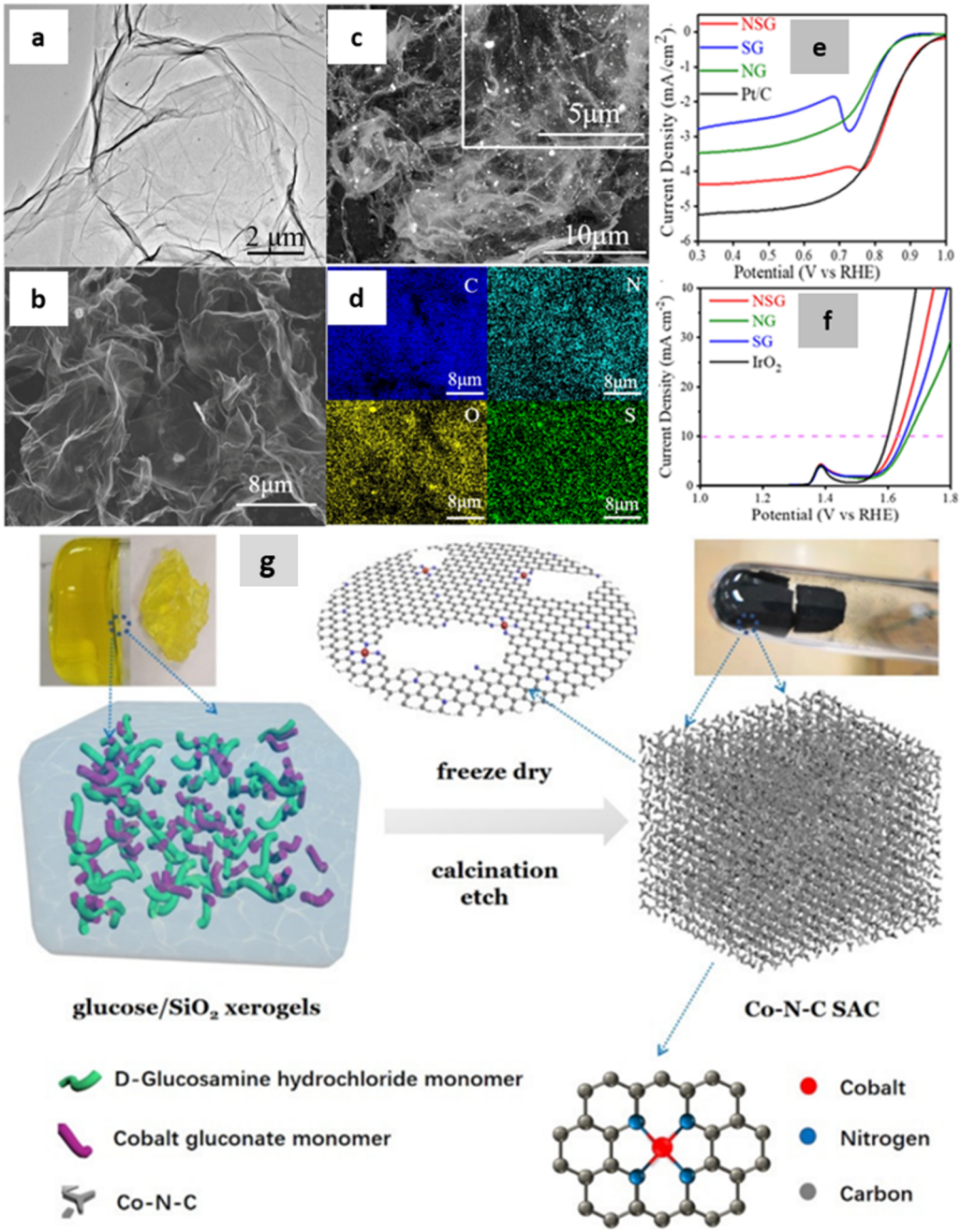


Figure 3: Transmission electron microscopy (TEM) (a), scanning electron microscopy (SEM) (b, c) and mapping (d) of different elements for NSG. (e) ORR linear sweep voltammograms of various catalysts along with Pt/C in O_2-saturated 0.1 M KOH solution, respectively; (f) OER linear sweep voltammograms of different catalysts with the benchmark IrO_2 (Figure 3a–f was adapted from [64] (© J. Zhang et al., published by MDPI, Basel, Switzerland, distributed under the terms of the Creative Commons Attribution 4.0 International License, https://creativecommons.org/licenses/by/4.0) (g) Scheme for synthesis of Co–N–C SACs (Figure 3g was adapted from [65] (© L. Wang et al., published by MDPI, Basel, Switzerland, distributed under the terms of the Creative Commons Attribution 4.0 International License, https://creativecommons.org/licenses/by/4.0).

coupling through synergistic effects, thereby resulting into bifunctional electrocatalyst.

Strasser and co-workers in 2013 demonstrated a fast microwave-assisted solvothermal one-pot method to synthesise carbon-supported NiFe-LDH and Fe–N–C materials. They were synthesised by repetitive annealing and acid leaching. When these catalysts were mixed, the XRD revealed a two-phase system. The composite of the two individual catalysts, which previously were only showing good activity towards either OER or ORR now exhibited a low overpotential window for ORR/OER in 0.1 M KOH [66]. Alloying of two or more metals

causes changes in electron energies, remodelling the surface for better binding spots acting as active sites for electrocatalytic processes [67]. Aziz et al. designed an economical bifunctional electrocatalyst through heat treatment of PAN/PVP precursor nanofibres containing bimetallic nanoparticles and melamine. The schematic representation of the synthesis procedure is shown in Figure 4a. FeNi-CNT@CNF was tested in a ZAB as shown in Figure 4b. To compare the catalyst's behaviour in the ZAB, 20% Pt/C and RuO_2 (1:1) was also tested. It was found that both open-circuit voltage and power density for FeNi-CNT@CNF was larger, that is, 1.36 V (Figure 4d) and 118 mW·cm^{-2}, respectively, compared to the benchmark catalyst with 50 mW·cm^{-2} (Figure 4e). Also, the specific capacity at 10 mA·cm^{-2} was much higher for FeNi-CNT@CNF

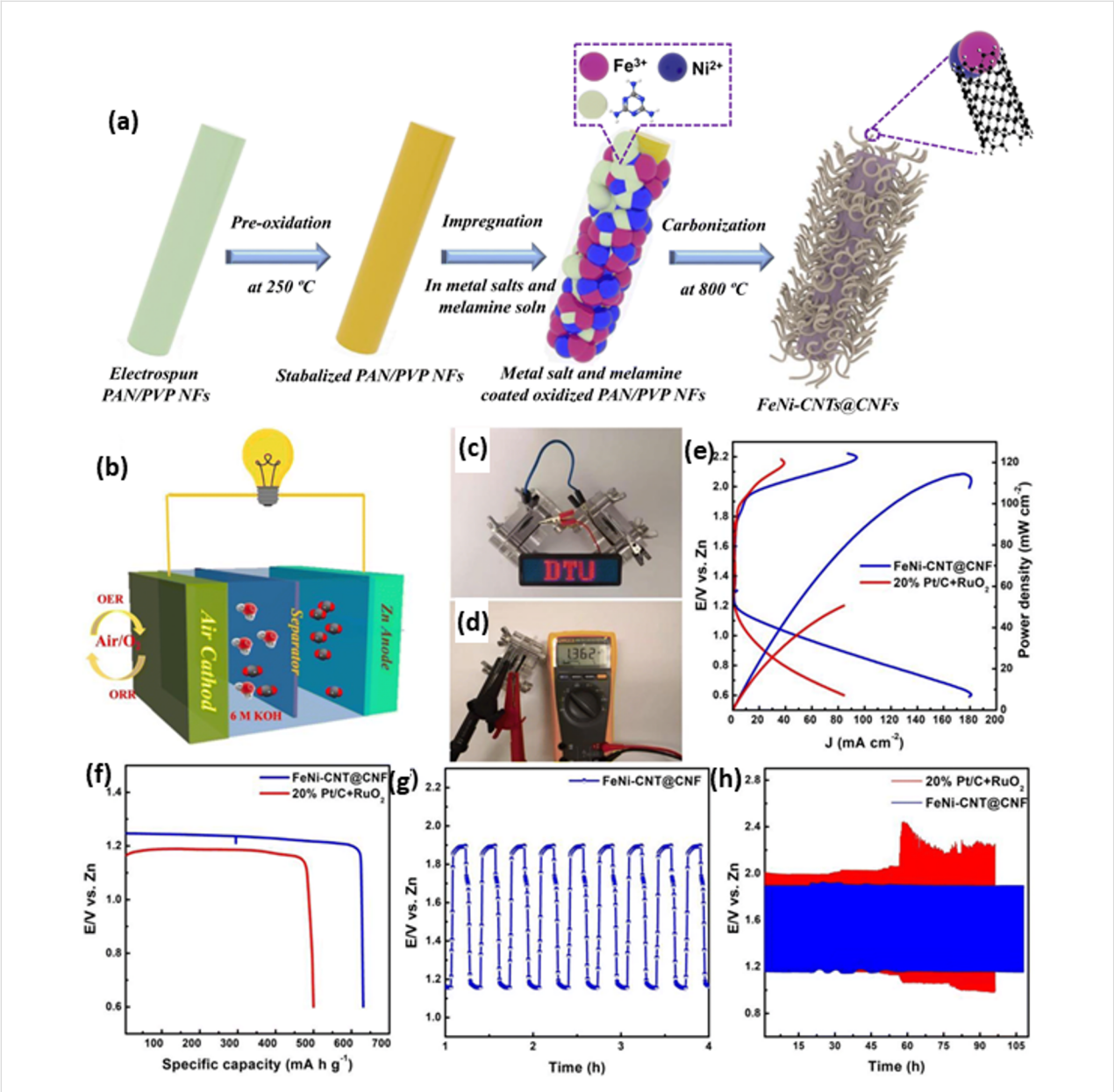


Figure 4: (a) A schematic illustrating the synthesis process of the FeNi-CNT@CNF nanocomposite is presented alongside (b) a visual depiction of the zinc–air battery (ZAB) structure. (c) A photograph of a light-emitting diode (LED, ≈3.0 V) powered by the ZAB demonstrates its operational capability. (d) The open-circuit voltage of the ZAB using the FeNi-CNT@CNF air cathode is shown, followed by (e) galvanodynamic discharge and power density performance. (f) Specific capacity data at a current density of 10 mA·cm^{-2} is also provided, along with (g, h) charge–discharge cycling behaviour of the FeNi-CNT@CNF electrode compared with a 20% Pt/C + RuO_2-based cathode under identical conditions. (Figure 4 was adapted from [68] ("Growth of carbon nanotubes over carbon nanofibers catalyzed by bimetallic alloy nanoparticles as a bifunctional electrode for Zn–air batteries" © 2023 I. Aziz et al., published by Royal Society of Chemistry, distributed under the terms of the Creative Commons Attribution NonCommercial 3.0 Unported License, https://creativecommons.org/licenses/by-nc/3.0/): This content is not subject to CC BY 4.0).

(Figure 4f), and the charge/discharge voltage gap at 5 mA·cm^{-2} for 108 h was found to be smaller than that of Pt/C catalyst [68]. Similarly, Yoo and co-workers reported a highly reversible bifunctional electrocatalyst, namely, NiFe alloy nanoparticles confined in CNTs on biaxially stretchable carbon cloth. It showed exceptional mechanical stability and rate performance, which makes it potential candidate for next-generation flexible devices [69].

The use of metal–organic frameworks as templates for synthesizing carbon-based electrocatalytic materials has gained significant momentum lately. This is due to their eco-friendliness, diverse structures, larger surface area, tunability, and high porosity, which ultimately support effective transfer of charges and boost performance [70]. Chen et al. developed a hierarchical architecture composite, that is, Co-NC@LDH, as an excellent bifunctional electrocatalyst. The catalyst contained NiFe-LDH nanosheets which were OER-active, harboured among ORR-active Co-doped CNTs on the surface of ZIF-derived carbon framework sheets. The corresponding potential difference, ΔE = 819 mV, is superior to the state of the art. This can be attributed to the LDH nanosheets and CNTs well distributed on the carbon framework while exposing plentiful active sites for both reactions [71]. Another work based on MOFs was done by Li and co-workers, where a honeycomb-like composite was fabricated by pyrolysis of a single-crystal Fe-MOF precursor. The composite showed promising results in a ZAB, and a 2.4 V LED light was powered for more than 24 h by integrating two ZABs [72].

Transition metal-based materials

Non-noble TMs, like Mn, Fe, Co, Ni, and Zn, are easily available elements, which show activity towards OER and ORR. After modification and optimization, the d orbitals may yield great electron transport efficiency and an excellent electronic structure to the catalyst. Researchers have created numerous superior catalyst materials that contain TMs [73,74]. The most recent developments in TM-based OER/ORR catalysts such as transition metal oxides (TMOs), mix-metal oxides (MMOs), sulfides, carbides, nitrides, and selenides are presented in this section.

The active sites on the catalyst surface for ORR and OER are particularly different, which is the main challenge in this research field [75,76]. Thus, finding the right active sites and controlling the intrinsic activity are essential to obtain high bifunctional performance. In addition, the electrocatalysts' structural characteristics ought to be adjusted to increase their surface area, speed up electron transfer and mass diffusion, and reveal more active sites that are involved in the catalytic process [77,78]. In order to improve the apparent electrocatalytic performances, the development of active catalysts with advantageous structures and high bifunctional intrinsic activity remains a key research priority.

Transition metal oxides. Based on encouraging experimental results, TMs and TMOs are viewed as another type of materials for ORR/OER [79]. To increase the conductivity, metals can be doped in the TMOs structure to create metal-doped TMOs; alternatively, they can be utilized directly as support for electrocatalysts in conjunction with a noble metal [76]. Good ORR performance of TMO-based catalysts is made possible by the presence of lower oxidation states of the TMOs and elements to mix with other active materials. However, under alkaline conditions, TMOs have also demonstrated exceptional efficacy regarding OER [80]. Electrical conductivity, crystal structure (crystallinity and terminating facets), morphology, surface chemistry, and metal valence state all influence TMOs' electrocatalytic activity towards ORR/OER. TMOs often are semiconductors. Nevertheless, by altering the chemical composition and adding oxygen vacancies, the conductivity can be significantly raised (to the "metal" level) [81].

Manganese oxides. In photosynthesis, oxygen evolution takes place at the oxygen-evolving complex (OEC). Mono-μ-oxo bridges to the fourth Mn ion are discovered to be present in this complex, which is composed of cuban-like Mn_3CaO_4 clusters [82]. According to calculations using DFT, every stage of the OER in these materials appears to be nearly thermoneutral, which is necessary for reversible catalysis [83,84]. Therefore, materials based on manganese have the potential to be intriguing bifunctional electrocatalysts for ORR/OER. Furthermore, their low price and excellent stability under alkaline conditions for ORR/OER have garnered a lot of interest lately. Mosa et al. evaluated the effect of the calcination temperature of Cs-doped manganese oxide (CsMnOx), which was produced using a simple soft-templated inverse micelle method. They found that 450 °C was the ideal calcination temperature [85]. Specifically, in the ORR, Cs-MnOx-450 follows the 4e$^-$ transfer pathway with a Tafel slope of 69 mV·dec^{-1}, which is close to the benchmark Pt/C catalyst. In the OER, Cs-MnOx-450 had a Tafel slope of 100 mV·dec^{-1} and 40 mA·cm^{-2} current density at 2.71 V vs RHE. This excellent catalytic activity was achieved by incorporation of Cs in the Mn_2O_3 structure. The presence of Cs increased the crystallinity of the material (via larger interparticle voids in the densely packed Mn_2O_3 structure) and stabilized the active Mn^{3+} ions on the surface responsible for ORR and OER.

Shao et al. enhanced Mn_2O_3's catalytic activity by combining two NiO and Mn_2O_3 through a straightforward chemical procedure, where carbon dots (CDs) were covalently linked with NiO

and Mn_2O_3 (NiO–Mn_2O_3-CDs). The material exhibited n = 3.85 and $j_d \approx 6$ mA·cm^{-2} for ORR, which is close to Pt-based electrocatalysts [86]. NiO–Mn_2O_3-CDs yielded 10 mA·cm^{-2} in the OER scenario with 298 mV overpotential and a Tafel slope of 141.14 mV·dec^{-1}. The oxygen-containing groups of the CDs are responsible for rapid exposure of the active sites and accelerated charge transfer by covalently bridging the Ni and Mn atoms.

Recently, Ayyaluri et al. used a simple one-step hydrothermal process without calcination to create manganese cobalt oxide/manganese oxide ($MnCo_2O_4/Mn_2O_3$) nanorods (NRs). The $MnCo_2O_4/Mn_2O_3$ NRs showed superior electrocatalytic capabilities for ORR and OER. In comparison to the Pt/C and IrO_2 catalysts, the $MnCo_2O_4/Mn_2O_3$ NR electrocatalyst demonstrated higher durability and high diffusion-limiting current density values. It exhibited remarkable durability across a range of current densities, showing only slight declines in potential. Additionally, it maintained stable chronopotentiometric performance for 30 h under a constant current density of 10 mA·cm^{-2}. Besides, compared to the Pt/C//IrO_2-based ZAB, the $MnCo_2O_4/Mn_2O_3$ NR-based ZAB showed a marginally smaller voltage plateau and lower electrochemical impedance values. Notably, the longevity of the $MnCo_2O_4/Mn_2O_3$ NR-based ZAB (68 cycles @ about 20.3 h) was superior to that of the Pt/C//IrO_2-based ZAB (28 cycles @ approximately 8.3 h) (Figure 5 shows the catalytic activity and stability of $MnCo_2O_4/Mn_2O_3$ NR compared to other catalysts) [87].

Cobalt oxides. Compared to other metal oxides, cobalt oxides perform reasonably well in ORR and OER, and their potential for enhancement through various synthesis techniques has made them a popular choice for bifunctional catalyst research [88,89]. Even though the precise mechanism of the catalytic active site is unknown, it has been shown that the higher OER activity is related higher levels of Co^{3+} oxidation states and that the ORR activity is related to higher levels of Co^{2+} oxidation states [90]. By tuning the ratio of Co^{2+} and Co^{3+} by different synthesis process, better bifunctional electrocatalysts towards ORR and OER can be developed.

Using a "carbonization–solvothermal–calcination" technique, He et al. prepared a CoO@NC catalyst, which showed excellent bifunctional performance. The CoO@NC-driven zinc–air battery outperforms commercial Pt/C-RuO_2 catalysts with an impressive peak power density of 112.4 mW·cm^{-2} and operates

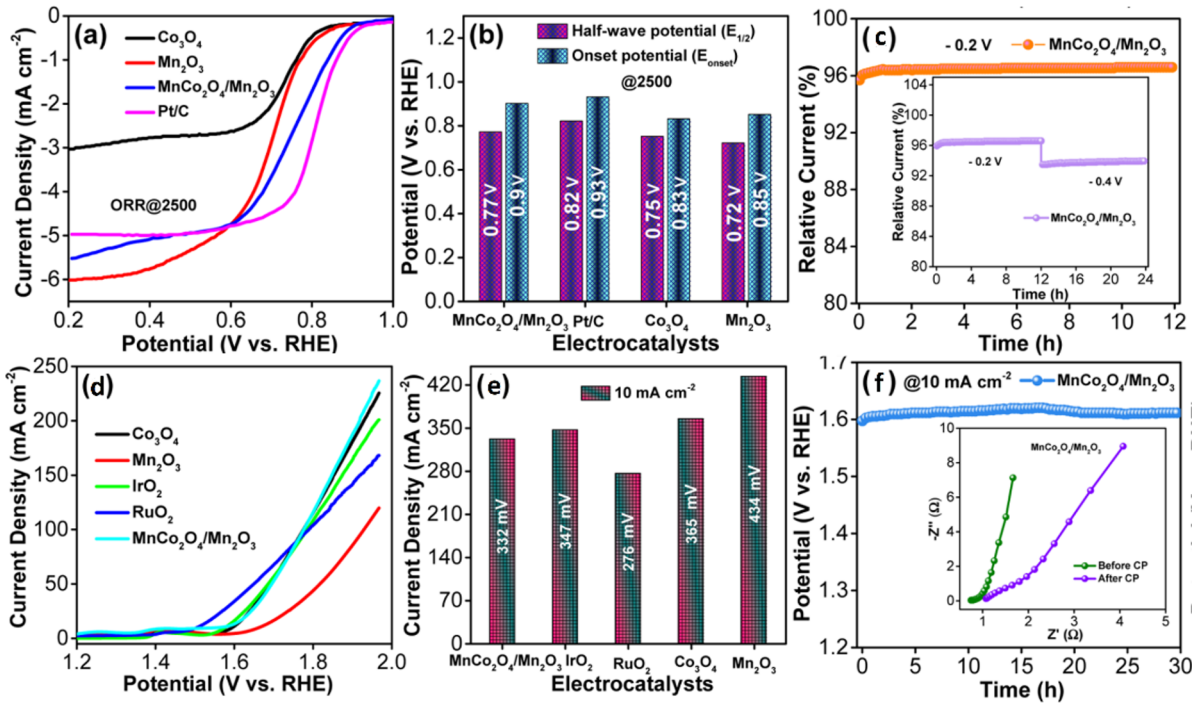


Figure 5: (a) Comparative ORR curves of the $MnCo_2O_4/Mn_2O_3$ NR, Mn_2O_3, Co_3O_4, and Pt/C catalysts at a fixed rotation of 2500 rpm. (b) Onset and half-wave potentials. (c) CA stability test results of the $MnCo_2O_4/Mn_2O_3$ NR electrocatalyst at a fixed voltage (–0.2 V) (inset of (c): at different voltages (–0.2 and –0.4 V) in a 0.1 M KOH electrolyte at a fixed rotation of 2500 rpm). (d) Comparative OER curves of the $MnCo_2O_4/Mn_2O_3$ NR, Mn_2O_3, Co_3O_4, IrO_2, and RuO_2 catalysts. (e) Overpotentials of the $MnCo_2O_4/Mn_2O_3$ NR, Mn_2O_3, Co_3O_4, IrO_2, and RuO_2 catalysts at the current densities of 10 mA·cm^{-2}. (f) CP stability test results of the $MnCo_2O_4/Mn_2O_3$ NR electrocatalyst at 10 mA·cm^{-2} (inset: EIS plot). (Figure 5 was adapted with permission from [87]. Copyright 2024 American Chemical Society).

consistently for over 200 h [91]. Ashok et al. reported a single-step solution combustion method to create porous $NiCoO_2$. In the ORR, 3.86 electrons were exchanged and a current density of 3.5 mA·cm^{-2} was achieved [92]. The catalyst was stable up to 24 h for OER with a Tafel slope of 95 mV·dec^{-1}. Oxygen vacancies and higher oxidation states are responsible for $NiCoO_2$'s higher activity and stability. A dandelion-shaped $NiCoO_2$ ($NiCo_2O_4$-DL) catalyst was examined by Liu et al. for alkaline ORR [93]. A 4e$^-$ ORR mechanism is indicated by the exchange of 3.91 electrons, with 3.9 mA·cm^{-2} current density. The numerous active Co^{3+} sites, high specific surface area, and three-dimensional porous structure are responsible for the good catalytic performance.

For an effective and long-lasting rechargeable ZAB application, Huang and co-workers recently synthesized a layered cobalt oxide $Ba_2Co_9O_{14}$ (BCO) via ball-milling [94]. Ball-milling effectively enhances the material's surface area, which contributes to a notable improvement in its catalytic efficiency for both ORR and OER under alkaline conditions. Furthermore, the synthesized BCO-based ZAB demonstrated a high specific capacity of 789 mAh g^{-1}, exceptional cycling stability exceeding 250 h at a current density of 10 mA·cm^{-2} with more than 1500 charge–discharge cycles, and a significantly elevated peak power density of 166 mW·cm^{-2}.

Nickel oxides. Nickel oxide (NiO) is p-type semiconductor, which has long been studied for OER because of its low resistance. It is unstable in acidic medium and can perform better under alkaline conditions [95]. For this reason, researchers are working hard to create and enhance the activity for OER in alkaline medium. Zhang et al. reported a waxberry-shaped cobalt–nickel oxide/S, N-codoped carbon hollow nanocomposites ($CoNiO_2$/SNC) as bifunctional catalysts. $CoNiO_2$/SNC required an overpotential of 381 mV to maintain 10 mA·cm^{-2} current density for OER. Also, it has a low Tafel slope of 34 mV·dec^{-1}. For ORR, $CoNiO_2$/SNC has a positive onset potential and a half wave potential of 0.85 and 0.70 V, respectively. Also, $CoNiO_2$/SNC has 6.5 mA·cm^{-2} diffusion-limited current density at 1600 rpm for ORR [96]. Faisal and co-workers reported an excellent bifunctional nickel/nickel oxide (Ni/NGr) catalyst supported on nitrogen-doped graphene [97]. For ORR, it has positive onset potential of 0.82 V and 5.0 mA·cm^{-2} current density at 2000 rpm. While for OER, the potential for 10 mA·cm^{-2} current density Ni/NGr is 1.62 V; also, it has a low Tafel slope of 98 mV·dec^{-1} [97].

Zhang et al. recently developed a copper-doped nickel oxide catalyst (Cu_x-NiOSC) via a coprecipitation technique for application in both oxygen reduction and evolution reactions [98]. The $Cu_{0.2}$-NiOSC catalyst displayed a Tafel slope of 57.8 mV·dec^{-1} during the ORR, along with an electron transfer number of approximately 3.6. In the context of the OER, this catalyst achieved a low overpotential of 510 mV at a current density of 10 mA·cm^{-2}. Notably, it also exhibited the lowest ΔE value of 0.93 V, indicating its superior bifunctional catalytic efficiency.

Regarding their abundant active sites, tunable electronic properties, and structural versatility, transition metal oxide catalysts have become very promising and affordable substitutes for noble-metal catalysts in OER and ORR. Because of the favourable adsorption energies of oxygen intermediates (*OH, *O, *OOH) and the formation of high-valence metal active species during operation, transition metal oxides, especially those based on Ni, Co, Fe, Mn, and their mixed oxides (e.g., spinels and perovskites), exhibit excellent activity for OER. In ORR, oxides like MnO_2, Co_3O_4, and perovskite-type materials exhibit competitive activity in alkaline media through improved electron transfer pathways and better oxygen binding, despite typically having poorer conductivity than carbides or nitrides. Catalytic kinetics and durability are greatly enhanced by techniques including defect engineering (defects like cation or anion vacancies can shift the metal's d-band centre relative to the Fermi level, which tunes the adsorption energy between catalyst surface and oxygen intermediates), morphology engineering (by controlling the physical shape, size and dimensionality, electrochemically active surface area can be maximized), heterojunction engineering (coupling of two or more distinct materials can modulate the d-band centre and provides dual-function active sites), vacancy engineering (creating metal or oxygen vacancies can change the electronic structure of the catalyst by redistributing electrons to neighbouring atoms, which modulates the conductivity), and composite formation with conductive carbon. Overall, transition metal oxides are moderately active for ORR and very effective for OER, especially in alkaline solutions. The development of good bifunctional oxide catalysts depends on ongoing interface engineering and electronic structure manipulation.

Transition metal non-oxide materials. As discussed above, researchers have extensively explored the bifunctional catalytic nature of TMO-based catalysts for OER/ORR. In recent years, researchers are also focussing on transition metal non-oxide electrocatalysts such as metal carbides, metal nitrides, metal sulfides, and metal selenides. They are of relevance to both OER and ORR because to their distinct shapes and surface properties.

An important class of interstitial alloys are transition metal carbides (TMCs), which are formed when carbon atoms dissolve interstitially into parent metal atom lattices. They have

unique physicochemical characteristics. They have high melting points, good thermal and electrical conductivities and extreme hardness. Because of these benefits, a variety of metal carbides, including cobalt, tungsten, and iron, have drawn increased interest as OER/ORR electrocatalysts [99,100]. Doping with heteroatoms such as N, B, P, and S is a commonly used approach to boost performance towards the ORR since it exposes active sites and increases conductivity [101,102]. N and B-codoped Co_3C (Co_3C-NB) was created by Ma et al. as an oxygen electrode in ZABs. Co_3C-NB's charge and discharge polarization curves, together with the power density curves, show that the cathode produces a greater power density than Pt/C + IrO_2 (36.8 mW·cm^{-2} at 100 mA·cm^{-2}), with 45.2 mW·cm^{-2} at 169.4 mA·cm^{-2} [103]. Similarly, Yang et al. reported Fe/Fe_3C encapsulated in carbon nanotubes, which had a reduced overpotential of 353 mV in OER and bifunctional activity of 0.86 V (vs RHE) for ORR [104].

Transition metal nitrides (TMNs) are also interstitial alloys similar to TMCs. The addition of nitrogen to the interstitial location modifies the parent metal structure. Ionic, covalent, and metallic bonds can develop between metal and nitrogen. TMCs have exceptional stress tolerance, hardness, and high brittleness. Due to strong hybridization between the transition metal d orbitals and nitrogen 2p orbitals, d-band contraction occurs in TMNs. Because of this, TMNs are more conductive than the corresponding metal oxides [105,106]. These characteristics led to increased interest in different transition metal nitride-based electrocatalysts for a range of electrochemical processes and ZAB applications. In 2019, Chen et al. prepared well-dispersed spherical Co_4N nanocrystals (Co_4N@NC) using melamine. Its electrochemical performance displays a half wave potential of 0.87 V. Additionally, at a current density of 10 mA·cm^{-2}, Co_4N@NC shows an OER overpotential of 398 mV. With this electrode, the ZAB yields a power density of 98.6 mW·cm^{-2} at 150 mA·cm^{-2} [107]. Wang et al. created Ni_3FeN/Co,N-CNF by annealing at 400 °C in an NH_3 environment. Ni_3FeN/Co,N-CNF outperforms commercial IrO_2 and Pt/C in terms of overpotential, achieving 270 mV for OER and 0.81 V for ORR, while maintaining the face-centred structure. Furthermore, the Ni_3FeN/Co,N-CNF cathode had 200 mW·cm^{-2} power density in a ZAB [108]. Yin and co-workers reported NiO/CoN nanowires, which had outstanding catalytic performance because of their many NiO and CoN nanointerfaces with plenty of vacancies, which can increase the catalyst's stability and catalytic performance. This battery had 945 Wh·kg^{-1} energy density and 79.6 mW·cm^{-2} power density while producing 200 mA·cm^{-2} current density [109].

Table 2 presents a comparison of various parameters related to the performance of the ORR and OER including its performance in ZABs for non-precious bifunctional electrocatalysts described in past few years [110-122].

Recently, Sanchez et al. reported Ni and Co-doped MnS_x (NCMS/NrGO) supported on N-doped reduced graphene which showed catalytic activity towards the ORR with E_{onset} of 0.94 V vs RHE with a Tafel slope of 27 mV·dec^{-1}. NCMS/NrGO required a potential of 1.59 V vs RHE to maintain 10 mA·cm^{-2} current density for OER. Additionally, it functions as a very effective air cathode for useful zinc–air batteries with long catalyst durability (1560 cycles, approximately 260 h) and high-power densities (124 mW·cm^{-2}) [123]. Peng and co-workers synthesized nitrogen-doped hollow carbon spheres (NHCS) loaded in $Ni_{0.85}Se$/$Co_{0.85}Se$ with 1:1 mass ratio $Ni_{0.85}Se$/$Co_{0.85}Se$-NHCS-2 for OER and ORR. $Ni_{0.85}Se$/$Co_{0.85}Se$-NHCS-2 demonstrated outstanding ORR activity, with a current density of 4.66 mA·cm^{-2}, an onset potential of 0.90 V, and a half-wave potential of 0.77 V. $Ni_{0.85}Se$/$Co_{0.85}Se$-NHCS-2 showed a Tafel slope of 118.3 mV·dec^{-1} and an operational potential of 1.63 V at a current density of 10 mA·cm^{-2} for OER activity, which is somewhat lower than that of RuO_2 (1.59 V) [124]. A composite of multiwalled carbon nanotubes (MWCNTs) and MnSe (MnSe@MWCNT) was reported by Singh et al. as bifunctional oxygen electrode. The MnSe@MWCNT catalyst composite surpasses state-of-the-art RuO_2, with a small Tafel slope of 54.76 mV·dec^{-1} with a very low overpotential of 290 mV at 10 mA·cm^{-2} along with E_{onset} of 0.94 V for ORR [125].

Because of their numerous active sites, high conductivity, and tunable electronic structures, transition metal carbides, nitrides, sulfides, and selenides have become effective non-noble metal electrocatalysts for the OER and ORR. Although carbides may experience surface oxidation under extreme OER circumstances, metal carbides and nitrides have substantial ORR activity and good bifunctional potential due to their metallic conductivity and advantageous d-band properties. During OER, metal nitrides frequently experience surface reconstruction to produce active oxyhydroxide species, which improves their stability and catalytic activity under alkaline conditions. The true active phases for OER are metal sulfides and selenides, which exhibit rich redox chemistry and easy surface transformation into metal (oxy)hydroxides. Selenides typically have better conductivity and charge transfer than sulfides, which leads to superior OER and competitive ORR performance. Overall, carbides and nitrides are particularly promising for ORR due to their conductivity and electronic structure, while sulfides and selenides excel in OER through in situ surface reconstruction; rational design strategies such as heterostructure engineering, defect creation, and heteroatom doping are key to achieving highly efficient and durable bifunctional ORR/OER catalysts.

Table 2: Comparison of bifunctional electrocatalysts for ORR and OER performance.

Electrocatalyst	ORR half-wave potential (in 0.1 M KOH)	OER overpotential at 10 mA·cm^{-2} (in 1 M KOH)	Performance in devices such as ZABs in terms of:				Ref.
			Specific Capacity (mA·h·g^{-1})	Power density (mW·cm^{-2})	Stability		
					time (h)	cycles	
NiFe-DG	0.86 V	358 mV	–	148	12	–	[59]
CoFe@($Co_{0.5}$ $Fe_{0.5}$)S@NCNT	0.88 V	266 mV	–	136.0	166	800	[63]
FeCo-1/NSC	0.82 V	325 mV	–	162.74	150	–	[67]
FeNi-CNT@CNF	0.80 V	310 mV	–	118	108	–	[68]
NiFe–N-CNT-KCC	0.87 V	173 mV	556.54	112.3	90	–	[69]
Co-NC@LDH	0.80 V	389 mV	806	107.8	300	1800	[71]
FeS/Fe_3C@NS-C-900	–	270 mV	750	90.9	865	1730	[72]
NiO-Mn_2O_3-CDs	0.84 V	298 mV	–	287	8.3	50	[86]
$Ba_2Co_9O_{14}$	0.71 V	–	789	166	250	1500	[94]
Ni-Co oxide (NC-2)	0.85 V	–	714	–	80	–	[110]
L-Co-NiO@CNT/CC	–	350 mV	756	73.4	960	–	[111]
CoO/NBC	–	–	676.1	127.2	–	400	[112]
$NiCo_2O_4$/MC-HT-O_2	0.76 V	621 mV	824.86	36.89	–	100	[113]
Co/MnO@NC	0.80 V	354 mV	–	217.7	459	–	[114]
N-MnO_x-30	0.80 V	–	841.71	181.15	13.8	–	[115]
Mn-Co_3O_4@CNTs	0.84 V	356 mV	–	116	425	1200	[116]
(Fe,Co)Se_2@Fe_1/NC	0.88 V	266 mV	775	260	280	1500	[117]
c-$CoSe_2$-CoN/NC	0.85 V	320 mV	802	118	250	–	[118]
A-Fe_3C@NO-PC	0.85 V	420 mV	–	136.9	52	300	[119]
Se-doped MOF CoS_2	0.88 V	290 mV	620.6	–	–	500	[120]
$Fe_{1.2}(CoNi)_{1.8}S_6$ MES	0.81 V	246 mV	–	124	300	–	[121]
Ni–Fe–MoN	0.72 V	228 mV	–	118	20	–	[122]

Conclusion

The development of OER/ORR non-precious bifunctional electrocatalysts for electrochemical conversion and storage devices greatly simplifies systems and cuts down the cost regarding commercialisation. However, for bifunctional electrocatalysts, the performance indicators for both reactions need to be taken into account equally, which is challenging. In this contribution, carbon- and transition metal-based materials as bifunctional oxygen electrocatalysts have been reviewed. The carbon-based catalysts have advantages, that is, abundance in nature, structural diversity, environmental compatibility, and high conductivity. However, only a very small number of carbon-based materials without any inclusion of transition metals have been tested for practical application. Many transition metal/carbon composites have been reported as electrocatalysts to show better activity than commercial ones (Pt/Ru/Ir based) in alkaline medium and have also been tested in devices like ZABs regarding stability/durability in practical settings. The activity of non-precious electrocatalysts in acidic medium has quite a lot of room of improvement. The catalysts' activities towards ORR/OER in acidic medium can be then compared with one of the studies done by Ruck et al. who deposited Ir on Pt black nanoparticles to obtain a bifunctional catalyst for acidic media [126]. Also, durability of the carbon-based catalyst at higher potentials (>1.2V vs RHE) for OER is quite a challenge as they are susceptible to corrosion. There is a lack of precise control of structure, composition, and active sites, which includes controlling the localization of the dopants in order to increase the activity of the electrocatalysts. Another vital parameter that is mostly ignored is catalyst degradation (including dissolution, oxidation, reconstruction, and carbon corrosion), which is a critical bottleneck for the practical deployment of bifunctional oxygen electrodes, especially under the alternating reducing and oxidizing conditions of ORR and OER. Additionally, study regarding bifunctionality will be more meaningful with in situ characterization and theoretical calculations to have a better understanding of the mechanistic pathway to determine the real active sites. Above all, since these catalysts are developed in laboratories, to check their compatibility with commercial scenarios, practical devices such as fuel cells and metal air batteries must be built. Some of the reported studies have carried out tests in ZAB-like devices, and this will be the ultimate requirement to verify whether a catalyst will be scalable or not for industrial levels.

In conclusion, this review intends to give an insight to the recent advances of non-precious metal bifunctional oxygen electrocatalysts. There is no doubt that there are advances in this field, and there are various design strategies to improve the activity of catalysts to a point where it can compete the state-of-the-art Pt/C, RuO_2, and IrO_2; however, further improvements are needed for commercial applications. We believe, the review could provide some useful insights for future progress in carbon or transition metal-based bifunctional oxygen electrocatalysts.

Funding

P.M.G. thankfully acknowledges DST, New Delhi for the Project Associate fellowship. P.B. acknowledges generous financial support from DST, New Delhi (PURSE Project No.: SR/PURSE/2024/240) and ANRF, New Delhi (project No.: CRG/2023/008294). S.P.B acknowledges ANRF, New Delhi for research fellowship. B.K.P and D.J.G. thanks UGC, New Delhi and CSIR, New Delhi for research fellowships, respectively.

Author Contributions

Shaheen Parveez Bhuyan: conceptualization; formal analysis; resources; writing – original draft; writing – review & editing. Bhrigu Kumar Pegu: conceptualization; resources; writing – original draft; writing – review & editing. Darshan Jyoti Gogoi: conceptualization; resources; writing – original draft; writing – review & editing. Pragya Moni Gogoi: conceptualization; resources; writing – original draft; writing – review & editing. Pankaj Bharali: conceptualization; funding acquisition; resources; supervision; writing – original draft; writing – review & editing.

ORCID® iDs

Pankaj Bharali - https://orcid.org/0000-0003-3471-0468

Data Availability Statement

Data sharing is not applicable as no new data was generated or analyzed in this study.

References

1. Pegis, M. L.; Wise, C. F.; Martin, D. J.; Mayer, J. M. *Chem. Rev.* **2018,** *118,* 2340–2391. doi:10.1021/acs.chemrev.7b00542
2. Wei, J.; Li, H.; Liu, Y.; Xie, W. *Langmuir* **2026,** *42,* 3997–4009. doi:10.1021/acs.langmuir.5c05473
3. Zhu, M.; Luo, H.; Bao, H.; Pan, Z.; Zhang, S.; Li, Z.; Zhang, D. *ACS Appl. Mater. Interfaces* **2026,** *18,* 1874–1884. doi:10.1021/acsami.5c23387
4. Wei, C.; Rao, R. R.; Peng, J.; Huang, B.; Stephens, I. E. L.; Risch, M.; Xu, Z. J.; Shao-Horn, Y. *Adv. Mater. (Weinheim, Ger.)* **2019,** *31,* 1806296. doi:10.1002/adma.201806296
5. Yuan, Y.; Zhong, X.; Chen, L.; Wang, R.; Xu, Z. *ACS Appl. Mater. Interfaces* **2026,** *18,* 6756–6768. doi:10.1021/acsami.5c19514
6. Huang, Z.-F.; Wang, J.; Peng, Y.; Jung, C.-Y.; Fisher, A.; Wang, X. *Adv. Energy Mater.* **2017,** *7,* 1700544. doi:10.1002/aenm.201700544
7. Wu, X.; Chen, F.; Jin, Y.; Zhang, N.; Johnston, R. L. *ACS Appl. Mater. Interfaces* **2015,** *7,* 17782–17791. doi:10.1021/acsami.5b04061
8. Suntivich, J.; Gasteiger, H. A.; Yabuuchi, N.; Nakanishi, H.; Goodenough, J. B.; Shao-Horn, Y. *Nat. Chem.* **2011,** *3,* 546–550. doi:10.1038/nchem.1069
9. Wei, X.; Cao, S.; Xu, H.; Jiang, C.; Wang, Z.; Ouyang, Y.; Lu, X.; Dai, F.; Sun, D. *ACS Mater. Lett.* **2022,** *4,* 1991–1998. doi:10.1021/acsmaterialslett.2c00694
10. Lim, C.; Fairhurst, A. R.; Ransom, B. J.; Haering, D.; Stamenkovic, V. R. *ACS Catal.* **2023,** *13,* 14874–14893. doi:10.1021/acscatal.3c03321
11. Majee, R.; Islam, Q. A.; Bhattacharyya, S. *ACS Appl. Mater. Interfaces* **2019,** *11,* 35853–35862. doi:10.1021/acsami.9b09299
12. Anantharaj, S.; Ede, S. R.; Sakthikumar, K.; Karthick, K.; Mishra, S.; Kundu, S. *ACS Catal.* **2016,** *6,* 8069–8097. doi:10.1021/acscatal.6b02479
13. Zheng, L.; Chen, G.; Huang, J.; Chen, W.; Han, T.; Li, T.; Ostrikov, K. K. *J. Colloid Interface Sci.* **2024,** *653,* 117–128. doi:10.1016/j.jcis.2023.09.046
14. Wang, Y.; Wu, Q.; Zhang, B.; Tian, L.; Li, K.; Zhang, X. *Catalysts* **2020,** *10,* 1164. doi:10.3390/catal10101164
15. Zeng, R.; Yang, Y.; Feng, X.; Li, H.; Gibbs, L. M.; DiSalvo, F. J.; Abruña, H. D. *Sci. Adv.* **2022,** *8,* eabj1584. doi:10.1126/sciadv.abj1584
16. Liu, J.; Xiao, J.; Luo, B.; Tian, E.; Waterhouse, G. I. N. *Chem. Eng. J.* **2022,** *427,* 132038. doi:10.1016/j.cej.2021.132038
17. Wei, L.; Ang, E. H.; Yang, Y.; Qin, Y.; Zhang, Y.; Ye, M.; Liu, Q.; Li, C. C. *J. Power Sources* **2020,** *477,* 228696. doi:10.1016/j.jpowsour.2020.228696
18. Wang, Y.-J.; Fang, B.; Zhang, D.; Li, A.; Wilkinson, D. P.; Ignaszak, A.; Zhang, L.; Zhang, J. *Electrochem. Energy Rev.* **2018,** *1,* 1–34. doi:10.1007/s41918-018-0002-3
19. Naik, K. M.; Sampath, S. *Electrochim. Acta* **2018,** *292,* 268–275. doi:10.1016/j.electacta.2018.08.138
20. Fu, G.; Tang, Y.; Lee, J.-M. *ChemElectroChem* **2018,** *5,* 1424–1434. doi:10.1002/celc.201800373
21. Hu, C.; Dai, L. *Angew. Chem., Int. Ed.* **2016,** *55,* 11736–11758. doi:10.1002/anie.201509982
22. Wang, J.; Kong, H.; Zhang, J.; Hao, Y.; Shao, Z.; Ciucci, F. *Prog. Mater. Sci.* **2021,** *116,* 100717. doi:10.1016/j.pmatsci.2020.100717
23. Mladenović, D.; Aykut, Y.; Yurtcan, A. B.; Soylu, G. S. P.; Santos, D. M. F.; Miljanić, Š.; Šljukić, B. *Processes* **2024,** *12,* 453. doi:10.3390/pr12030453
24. Jiao, Y.; Xu, K.; Xiao, H.; Mei, C.; Li, J. *Nanomaterials* **2023,** *13,* 2397. doi:10.3390/nano13172397
25. Ran, Y.; Xu, C.; Ji, D.; Zhao, H.; Li, L.; Lei, Y. *Nano Res. Energy* **2024,** *3,* e9120092. doi:10.26599/nre.2023.9120092
26. Marković, N. M.; Schmidt, T. J.; Stamenković, V.; Ross, P. N. *Fuel Cells* **2001,** *1,* 105–116. doi:10.1002/1615-6854(200107)1:2<105::aid-fuce105>3.0.co;2-9

27. Nørskov, J. K.; Rossmeisl, J.; Logadottir, A.; Lindqvist, L.; Kitchin, J. R.; Bligaard, T.; Jónsson, H. *J. Phys. Chem. B* **2004,** *108,* 17886–17892. doi:10.1021/jp047349j
28. Wang, K.; Liu, W.; Song, M.; Lu, Z.-H. *Rare Met.* **2026,** *45,* e70097. doi:10.1002/rar2.70097
29. Ma, R.; Lin, G.; Zhou, Y.; Liu, Q.; Zhang, T.; Shan, G.; Yang, M.; Wang, J. *npj Comput. Mater.* **2019,** *5,* 78. doi:10.1038/s41524-019-0210-3
30. Li, S.; Shi, L.; Guo, Y.; Wang, J.; Liu, D.; Zhao, S. *Chem. Sci.* **2024,** *15,* 11188–11228. doi:10.1039/d4sc02853h
31. Zhao, X.; Hao, Z.; Zhang, X.; Li, L.; Gao, Y.; Liu, L. *Chem. Eng. J.* **2024,** *497,* 155005. doi:10.1016/j.cej.2024.155005
32. Aghamohammadi, P.; Hüner, B.; Altıncı, O. C.; Akgul, E. T.; Teymur, B.; Simsek, U. B.; Demir, M. *Int. J. Hydrogen Energy* **2024,** *87,* 179–198. doi:10.1016/j.ijhydene.2024.08.412
33. Liu, M.; Wang, X.; Cao, S.; Lu, X.; Li, W.; Li, N.; Bu, X.-H. *Adv. Mater. (Weinheim, Ger.)* **2024,** *36,* 2309231. doi:10.1002/adma.202309231
34. Wang, Z.; Jin, X.; Zhu, C.; Liu, Y.; Tan, H.; Ku, R.; Zhang, Y.; Zhou, L.; Liu, Z.; Hwang, S.-J.; Fan, H. J. *Adv. Mater. (Weinheim, Ger.)* **2021,** *33,* 2104718. doi:10.1002/adma.202104718
35. Ge, X.; Sumboja, A.; Wuu, D.; An, T.; Li, B.; Goh, F. W. T.; Hor, T. S. A.; Zong, Y.; Liu, Z. *ACS Catal.* **2015,** *5,* 4643–4667. doi:10.1021/acscatal.5b00524
36. Yan, Z.; Liu, H.; Hao, Z.; Yu, M.; Chen, X.; Chen, J. *Chem. Sci.* **2020,** *11,* 10614–10625. doi:10.1039/d0sc01532f
37. Wang, T.; Zhang, Y.; Huang, B.; Cai, B.; Rao, R. R.; Giordano, L.; Sun, S.-G.; Shao-Horn, Y. *Nat. Catal.* **2021,** *4,* 753–762. doi:10.1038/s41929-021-00668-0
38. He, B.; Bai, F.; Jain, P.; Li, T. *Small* **2025,** *21,* 2411479. doi:10.1002/smll.202411479
39. Ivanistsev, V.; Cepitis, R.; Rossmeisl, J.; Kongi, N. *Chem. Soc. Rev.* **2025,** *54,* 10956–10976. doi:10.1039/d5cs00597c
40. Liu, H.; Xiong, R.; Ma, S.; Wang, R.; Liu, Z.; Yao, T.; Song, B. *Energy Adv.* **2025,** *4,* 55–83. doi:10.1039/d4ya00551a
41. Nsanzimana, J. M. V.; Peng, Y.; Xu, Y. Y.; Thia, L.; Wang, C.; Xia, B. Y.; Wang, X. *Adv. Energy Mater.* **2018,** *8,* 1701475. doi:10.1002/aenm.201701475
42. Wu, G.; Santandreu, A.; Kellogg, W.; Gupta, S.; Ogoke, O.; Zhang, H.; Wang, H.-L.; Dai, L. *Nano Energy* **2016,** *29,* 83–110. doi:10.1016/j.nanoen.2015.12.032
43. Zeng, K.; Zheng, X.; Li, C.; Yan, J.; Tian, J.-H.; Jin, C.; Strasser, P.; Yang, R. *Adv. Funct. Mater.* **2020,** *30,* 2000503. doi:10.1002/adfm.202000503
44. Wang, T.; Kou, Z.; Mu, S.; Liu, J.; He, D.; Amiinu, I. S.; Meng, W.; Zhou, K.; Luo, Z.; Chaemchuen, S.; Verpoort, F. *Adv. Funct. Mater.* **2018,** *28,* 1705048. doi:10.1002/adfm.201705048
45. Razzaq, S.; Exner, K. S. *ChemElectroChem* **2022,** *9,* e202101603. doi:10.1002/celc.202101603
46. Hou, S.; Kluge, R. M.; Haid, R. W.; Gubanova, E. L.; Watzele, S. A.; Bandarenka, A. S.; Garlyyev, B. *ChemElectroChem* **2021,** *8,* 3433–3456. doi:10.1002/celc.202100584
47. Wang, H.-F.; Tang, C.; Wang, B.; Li, B.-Q.; Cui, X.; Zhang, Q. *Energy Storage Mater.* **2018,** *15,* 124–130. doi:10.1016/j.ensm.2018.03.022
48. Bera, R. K.; Park, H.; Ryoo, R. *J. Mater. Chem. A* **2019,** *7,* 9988–9996. doi:10.1039/c9ta01482a
49. Jia, Y.; Chen, J.; Yao, X. *Mater. Chem. Front.* **2018,** *2,* 1250–1268. doi:10.1039/c8qm00070k
50. Hu, C.; Xiao, Y.; Zou, Y.; Dai, L. *Electrochem. Energy Rev.* **2018,** *1,* 84–112. doi:10.1007/s41918-018-0003-2
51. Xie, C.; Yan, D.; Chen, W.; Zou, Y.; Chen, R.; Zang, S.; Wang, Y.; Yao, X.; Wang, S. *Mater. Today* **2019,** *31,* 47–68. doi:10.1016/j.mattod.2019.05.021
52. Banks, C. E.; Davies, T. J.; Wildgoose, G. G.; Compton, R. G. *Chem. Commun.* **2005,** 829–841. doi:10.1039/b413177k
53. Su, C.; Acik, M.; Takai, K.; Lu, J.; Hao, S.-j.; Zheng, Y.; Wu, P.; Bao, Q.; Enoki, T.; Chabal, Y. J.; Ping Loh, K. *Nat. Commun.* **2012,** *3,* 1298. doi:10.1038/ncomms2315
54. Tao, L.; Qiao, M.; Jin, R.; Li, Y.; Xiao, Z.; Wang, Y.; Zhang, N.; Xie, C.; He, Q.; Jiang, D.; Yu, G.; Li, Y.; Wang, S. *Angew. Chem., Int. Ed.* **2019,** *58,* 1019–1024. doi:10.1002/anie.201810207
55. Li, M.; Zhang, L.; Xu, Q.; Niu, J.; Xia, Z. *J. Catal.* **2014,** *314,* 66–72. doi:10.1016/j.jcat.2014.03.011
56. Hu, C.; Dai, L. *Adv. Mater. (Weinheim, Ger.)* **2017,** *29,* 1604942. doi:10.1002/adma.201604942
57. Zhu, J.; Mu, S. *Adv. Funct. Mater.* **2020,** *30,* 2001097. doi:10.1002/adfm.202001097
58. Fan, L.; Xu, J.; Hong, Y. *RSC Adv.* **2022,** *12,* 6772–6782. doi:10.1039/d1ra08884j
59. Khan, K.; Yan, X.; Yu, Q.; Bae, S.-H.; White, J. J.; Liu, J.; Liu, T.; Sun, C.; Kim, J.; Cheng, H.-M.; Wang, Y.; Liu, B.; Amine, K.; Pan, X.; Luo, Z. *Nano Energy* **2021,** *90,* 106488. doi:10.1016/j.nanoen.2021.106488
60. Zhao, Z.; Li, M.; Zhang, L.; Dai, L.; Xia, Z. *Adv. Mater. (Weinheim, Ger.)* **2015,** *27,* 6834–6840. doi:10.1002/adma.201503211
61. Zong, L.; Wu, W.; Liu, S.; Yin, H.; Chen, Y.; Liu, C.; Fan, K.; Zhao, X.; Chen, X.; Wang, F.; Yang, Y.; Wang, L.; Feng, S. *Energy Storage Mater.* **2020,** *27,* 514–521. doi:10.1016/j.ensm.2019.12.013
62. Zhao, Q.; Bao, L.; Wang, H.; Dou, D.; Cong, Y.; Li, C. *Ionics* **2024,** *30,* 4797–4810. doi:10.1007/s11581-024-05478-5
63. Yang, J.; Shi, J.; Wu, Y.; Liu, H.; Liu, Z.; You, Q.; Li, X.; Cong, L.; Liu, D.; Liu, F.; Jiang, Y.; Lin, N.; Zhang, W.; Lin, H. *J. Mater. Chem. A* **2024,** *12,* 11907–11919. doi:10.1039/d4ta00555d
64. Zhang, J.; Wang, J.; Wu, Z.; Wang, S.; Wu, Y.; Liu, X. *Catalysts* **2018,** *8,* 475. doi:10.3390/catal8100475
65. Wang, L.; Xu, Z.; Peng, T.; Liu, M.; Zhang, L.; Zhang, J. *Nanomaterials* **2022,** *12,* 381. doi:10.3390/nano12030381
66. Dresp, S.; Luo, F.; Schmack, R.; Kühl, S.; Gliech, M.; Strasser, P. *Energy Environ. Sci.* **2016,** *9,* 2020–2024. doi:10.1039/c6ee01046f
67. Chang, S.; Zhang, H.; Zhang, Z. *J. Energy Chem.* **2021,** *56,* 64–71. doi:10.1016/j.jechem.2020.07.047
68. Aziz, I.; Chen, X.; Hu, X.; Zhang, W.; Awan, R. J.; Rauf, A.; Arshad, S. N. *RSC Adv.* **2023,** *13,* 11591–11599. doi:10.1039/d3ra00352c
69. Poudel, M. B.; Vijayapradeep, S.; Sekar, K.; Kim, J. S.; Yoo, D. J. *J. Mater. Chem. A* **2024,** *12,* 10185–10195. doi:10.1039/d3ta07609a
70. Adegoke, K. A.; Maxakato, N. W. *Mater. Today Energy* **2021,** *21,* 100816. doi:10.1016/j.mtener.2021.100816
71. Chen, D.; Chen, X.; Cui, Z.; Li, G.; Han, B.; Zhang, Q.; Sui, J.; Dong, H.; Yu, J.; Yu, L.; Dong, L. *Chem. Eng. J.* **2020,** *399,* 125718. doi:10.1016/j.cej.2020.125718
72. Li, Y.-W.; Zhang, W.-J.; Li, J.; Ma, H.-Y.; Du, H.-M.; Li, D.-C.; Wang, S.-N.; Zhao, J.-S.; Dou, J.-M.; Xu, L. *ACS Appl. Mater. Interfaces* **2020,** *12,* 44710–44719. doi:10.1021/acsami.0c11945

73. Suen, N.-T.; Hung, S.-F.; Quan, Q.; Zhang, N.; Xu, Y.-J.; Chen, H. M. *Chem. Soc. Rev.* **2017,** *46,* 337–365. doi:10.1039/c6cs00328a
74. Xue, Y.; Sun, S.; Wang, Q.; Dong, Z.; Liu, Z. *J. Mater. Chem. A* **2018,** *6,* 10595–10626. doi:10.1039/c7ta10569j
75. Kuang, M.; Zheng, G. *Small* **2016,** *12,* 5656–5675. doi:10.1002/smll.201600977
76. Khattak, K. N.; Shao, Y.; Zhou, J. *React. Chem. Eng.* **2026,** *11,* 11–41. doi:10.1039/d5re00328h
77. Wu, S.; Liang, Z.; Wang, T.; Liu, X.; Huang, S. *Inorg. Chem. Front.* **2025,** *12,* 848–875. doi:10.1039/d4qi02179g
78. Li, R.-J.; Niu, W.-J.; Zhao, W.-W.; Yu, B.-X.; Cai, C.-Y.; Xu, L.-Y.; Wang, F.-M. *Small* **2025,** *21,* 2408227. doi:10.1002/smll.202408227
79. Hou, A.; Ouyang, R. *ACS Appl. Energy Mater.* **2025,** *8,* 3481–3490. doi:10.1021/acsaem.4c03003
80. Yuan, C.; Wu, H. B.; Xie, Y.; Lou, X. W. *Angew. Chem., Int. Ed.* **2014,** *53,* 1488–1504. doi:10.1002/anie.201303971
81. Wang, Y.; Li, J.; Wei, Z. *J. Mater. Chem. A* **2018,** *6,* 8194–8209. doi:10.1039/c8ta01321g
82. Ferreira, K. N.; Iverson, T. M.; Maghlaoui, K.; Barber, J.; Iwata, S. *Science* **2004,** *303,* 1831–1838. doi:10.1126/science.1093087
83. Rossmeisl, J.; Dimitrievski, K.; Siegbahn, P.; Nørskov, J. K. *J. Phys. Chem. C* **2007,** *111,* 18821–18823. doi:10.1021/jp077210j
84. Gorlin, Y.; Jaramillo, T. F. *J. Am. Chem. Soc.* **2010,** *132,* 13612–13614. doi:10.1021/ja104587v
85. Mosa, I. M.; Biswas, S.; El-Sawy, A. M.; Botu, V.; Guild, C.; Song, W.; Ramprasad, R.; Rusling, J. F.; Suib, S. L. *J. Mater. Chem. A* **2016,** *4,* 620–631. doi:10.1039/c5ta07878d
86. Shao, C.; Liao, F.; Zhu, W.; Zhang, Y.; Ma, M.; Yang, J.; Yin, K.; Shao, M.; Jiang, B. *Appl. Surf. Sci.* **2022,** *596,* 153642. doi:10.1016/j.apsusc.2022.153642
87. Ayyaluri, R. R.; Vamsi Krishna, B. N.; Ankinapalli, O. R.; Lee, Y. J.; Natarajan, L.; Yu, J. S. *ACS Sustainable Chem. Eng.* **2024,** *12,* 10765–10775. doi:10.1021/acssuschemeng.4c01477
88. Wu, G.; Zelenay, P. *Acc. Chem. Res.* **2013,** *46,* 1878–1889. doi:10.1021/ar400011z
89. Lyu, C.; Yang, J.; Guo, H.; Cheng, J.; Geng, D.; Liu, Y. *Coord. Chem. Rev.* **2026,** *551,* 217393. doi:10.1016/j.ccr.2025.217393
90. Xiao, J.; Kuang, Q.; Yang, S.; Xiao, F.; Wang, S.; Guo, L. *Sci. Rep.* **2013,** *3,* 2300. doi:10.1038/srep02300
91. He, X.; Yin, F.; Li, G. *Int. J. Hydrogen Energy* **2015,** *40,* 9713–9722. doi:10.1016/j.ijhydene.2015.06.027
92. Ashok, A.; Kumar, A.; Ponraj, J.; Mansour, S. A.; Tarlochan, F. *Int. J. Hydrogen Energy* **2019,** *44,* 16603–16614. doi:10.1016/j.ijhydene.2019.04.165
93. Liu, Y.; Shu, C.; Fang, Y.; Chen, Y.; Liu, Y. *J. Power Sources* **2017,** *361,* 160–169. doi:10.1016/j.jpowsour.2017.06.062
94. Huang, D.; Liu, T.; Xu, A.; Zhou, J.; Wang, Y.; Hu, X. *Electrochim. Acta* **2024,** *494,* 144450. doi:10.1016/j.electacta.2024.144450
95. Farah Hanis Nik Zaiman, N.; Shaari, N. *J. Ind. Eng. Chem. (Amsterdam, Neth.)* **2023,** *119,* 1–76. doi:10.1016/j.jiec.2022.11.048
96. Zhang, Q.; Han, W.; Xu, Z.; Li, Y.; Chen, L.; Bai, Z.; Yang, L.; Wang, X. *RSC Adv.* **2020,** *10,* 27788–27793. doi:10.1039/d0ra03222k
97. Faisal, S. N.; Haque, E.; Noorbehesht, N.; Liu, H.; Islam, M. M.; Shabnam, L.; Roy, A. K.; Pourazadi, E.; Islam, M. S.; Harris, A. T.; Minett, A. I. *Sustainable Energy Fuels* **2018,** *2,* 2081–2089. doi:10.1039/c8se00068a
98. Zhang, J.; Zhuge, X.; Liu, T.; Luo, K.; Lyu, J.; Ren, Y.; Li, Y.; Xing, L. *Mater. Today Commun.* **2024,** *38,* 108335. doi:10.1016/j.mtcomm.2024.108335
99. Zhong, Y.; Xia, X.; Shi, F.; Zhan, J.; Tu, J.; Fan, H. J. *Adv. Sci.* **2016,** *3,* 1500286. doi:10.1002/advs.201500286
100. Kumar, D. B.; Nie, W.; Jiang, Z.; Lee, J.; Maiyalagan, T. *J. Alloys Compd.* **2023,** *960,* 170828. doi:10.1016/j.jallcom.2023.170828
101. Ram, S.; Lee, A. S.; Lee, S.-C.; Bhattacharjee, S. *Chem. Mater.* **2025,** *37,* 3608–3621. doi:10.1021/acs.chemmater.4c03213
102. Wang, L.; Dong, H.; Guo, Z.; Zhang, L.; Hou, T.; Li, Y. *J. Phys. Chem. C* **2016,** *120,* 17427–17434. doi:10.1021/acs.jpcc.6b04639
103. Ma, X.; Li, K.; Zhang, X.; Wei, B.; Yang, H.; Liu, L.; Zhang, M.; Zhang, X.; Chen, Y. *J. Mater. Chem. A* **2019,** *7,* 14904–14915. doi:10.1039/c9ta03762d
104. Yang, F.; Lei, Y.; Xie, H.; Zhang, D.; Huang, R.; Liu, X.; Wang, H. *New J. Chem.* **2020,** *44,* 10729–10738. doi:10.1039/d0nj01164a
105. Kindlund, H.; Sangiovanni, D. G.; Petrov, I.; Greene, J. E.; Hultman, L. *Thin Solid Films* **2019,** *688,* 137479. doi:10.1016/j.tsf.2019.137479
106. Tareen, A. K.; Priyanga, G. S.; Khan, K.; Pervaiz, E.; Thomas, T.; Yang, M. *ChemSusChem* **2019,** *12,* 3941–3954. doi:10.1002/cssc.201900553
107. Chen, L.; Zhang, Y.; Liu, X.; Long, L.; Wang, S.; Xu, X.; Liu, M.; Yang, W.; Jia, J. *Carbon* **2019,** *151,* 10–17. doi:10.1016/j.carbon.2019.05.063
108. Wang, Q.; Shang, L.; Shi, R.; Zhang, X.; Waterhouse, G. I. N.; Wu, L.-Z.; Tung, C.-H.; Zhang, T. *Nano Energy* **2017,** *40,* 382–389. doi:10.1016/j.nanoen.2017.08.040
109. Yin, J.; Li, Y.; Lv, F.; Fan, Q.; Zhao, Y.-Q.; Zhang, Q.; Wang, W.; Cheng, F.; Xi, P.; Guo, S. *ACS Nano* **2017,** *11,* 2275–2283. doi:10.1021/acsnano.7b00417
110. Gultom, N. S.; Silitonga, M. Z.; Hu, K.-X.; Zhou, Y.-C.; Kuo, D.-H. *J. Alloys Compd.* **2023,** *955,* 170232. doi:10.1016/j.jallcom.2023.170232
111. Park, Y. S.; Lee, J.; Lee, H.; Park, J. B.; Yun, J.; Lee, C. U.; Moon, S.; Lee, S.; Kim, S.; Kim, J. H.; Kim, D.; Han, J.; Kim, D.-W.; Moon, J. *ACS Appl. Mater. Interfaces* **2025,** *17,* 18228–18242. doi:10.1021/acsami.4c20630
112. Sun, Q.; Chen, Z.; Dong, K.; Lv, T.; Li, X.; Zhai, D.; Tang, W.; Chen, T. *J. Colloid Interface Sci.* **2025,** *692,* 137537. doi:10.1016/j.jcis.2025.137537
113. Díaz, C.; Moreno-Zuria, A.; Sfeir, A.; Royer, S.; Sierra, L.; López, B.; Mohamedi, M.; Palacio, R. *J. Energy Storage* **2025,** *126,* 117099. doi:10.1016/j.est.2025.117099
114. Wang, L.; Huang, J.; Hu, X.; Huang, Z.; Gao, M.; Yao, D.; Taylor Isimjan, T.; Yang, X. *J. Colloid Interface Sci.* **2024,** *660,* 989–996. doi:10.1016/j.jcis.2024.01.143
115. Zhang, D.; Yue, D.; He, C.; Ma, Z.; Wu, Q.; Huang, Y.; Liu, K.; Wang, H.; Cai, Y.; Li, Q. *J. Alloys Compd.* **2023,** *968,* 171924. doi:10.1016/j.jallcom.2023.171924
116. Zhang, X.; Liu, Q.; Liu, S.; Wang, E. *Electrochim. Acta* **2023,** *437,* 141477. doi:10.1016/j.electacta.2022.141477
117. Zheng, H.; Wang, S.; Liu, S.; Wu, J.; Guan, J.; Li, Q.; Wang, Y.; Tao, Y.; Hu, S.; Bai, Y.; Wang, J.; Xiong, X.; Xiong, Y.; Lei, Y. *Adv. Funct. Mater.* **2023,** *33,* 2300815. doi:10.1002/adfm.202300815
118. Xu, X.; Wang, X.; Huo, S.; Liu, X.; Ma, X.; Liu, M.; Zou, J. *Adv. Mater. (Weinheim, Ger.)* **2024,** *36,* 2306844. doi:10.1002/adma.202306844

119. Lai, J.; Gan, L.; Zhang, K.; Fang, J.; Lai, Y.; Li, J. *J. Electroanal. Chem.* **2020,** *873,* 114369. doi:10.1016/j.jelechem.2020.114369
120. Muthurasu, A.; Sampath, P.; Ko, T. H.; Lohani, P. C.; Pathak, I.; Acharya, D.; Chhetri, K.; Kim, D. H.; Kim, H. Y. *Appl. Catal., B* **2023,** *330,* 122523. doi:10.1016/j.apcatb.2023.122523
121. Wu, H.; Li, Z.; Wang, Z.; Ma, Y.; Huang, S.; Ding, F.; Li, F.; Zhai, Q.; Ren, Y.; Zheng, X.; Yang, Y.; Tang, S.; Deng, Y.; Meng, X. *Appl. Catal., B* **2023,** *325,* 122356. doi:10.1016/j.apcatb.2022.122356
122. Zhu, C.; Yin, Z.; Lai, W.; Sun, Y.; Liu, L.; Zhang, X.; Chen, Y.; Chou, S.-L. *Adv. Energy Mater.* **2018,** *8,* 1802327. doi:10.1002/aenm.201802327
123. Sanchez, J. S.; Xia, Z.; Mirehbar, K.; Sasidharan, S.; Aravindh, S. A.; Liscio, A.; Sun, J.; Christian, M.; Palma, J.; Palermo, V.; Marcilla, R. *J. Mater. Chem. A* **2024,** *12,* 11945–11959. doi:10.1039/d3ta07765a
124. Peng, L.-J.; Huang, J.-P.; Pan, Q.-R.; Liang, Y.; Yin, N.; Xu, H.-C.; Li, N. *RSC Adv.* **2021,** *11,* 19406–19416. doi:10.1039/d1ra02861h
125. Singh, H.; Marley-Hines, M.; Chakravarty, S.; Nath, M. *J. Mater. Chem. A* **2022,** *10,* 6772–6784. doi:10.1039/d1ta09864k
126. Ruck, S.; Hutzler, A.; Lahn, L.; Kasian, O.; Thiele, S.; Pham, C. v.; Freiberg, A. T. S. *ACS Catal.* **2025,** *15,* 3487–3498. doi:10.1021/acscatal.4c07208

License and Terms

This is an open access article licensed under the terms of the Beilstein-Institut Open Access License Agreement (https://www.beilstein-journals.org/bjnano/terms), which is identical to the Creative Commons Attribution 4.0 International License (https://creativecommons.org/licenses/by/4.0). The reuse of material under this license requires that the author(s), source and license are credited. Third-party material in this article could be subject to other licenses (typically indicated in the credit line), and in this case, users are required to obtain permission from the license holder to reuse the material.

The definitive version of this article is the electronic one which can be found at:
https://doi.org/10.3762/bjnano.17.90